Compound Drought and Heatwaves at a Global Scale: The Role of Natural Climate Variability- Associated Synoptic Patterns and Land-Surface Energy Budget Anomalies.

Sourav Mukherjee[1], Moetasim Ashfaq[2], Ashok Kumar Mishra[1]

[1]Glenn Department of Civil Engineering,

Clemson University, South Carolina, USA.

[2]Oak Ridge National Laboratory, Oak Ridge, USA

Corresponding author: Ashok Kumar Mishra (ashokm@g.clemson.edu)

Key points

- Associations between seasonal occurrences of compound drought and heatwave (CDHW) events and the major natural modes of climate variability are investigated.
- ENSO is the most influential natural mode of variability associated with the seasonal occurrences of CDHW events over tropical regions in the Southern Hemisphere.
- Anomalies in seasonal composites of pertinent variables explain most of these associations except for few regions.

Abstract

Compound drought and heatwave (CDHW) events have garnered much attention in recent studies. However, thus far, the identification of such events is oversimplified and their association with natural climate variability is not fully explored. Here, we derive anomalies in the weekly self-calibrated Palmer Drought Severity Index (sc_PDSI) and daily maximum temperatures to identify CDHW events from 1982 to 2016 over 26 climate regions across the globe. Using a Poisson Generalized Linear Model (GLM), we analyze yearly occurrences of seasonal CDHW events and their association with the warm and cold phases of El Nino Southern Oscillation (ENSO), Pacific Decadal Oscillation (PDO), and North Atlantic Oscillation (NAO). ENSO exhibits robust association with CDHW events over the Southern Hemisphere during the austral summer and fall, while PDO influences their occurrences over the Western North America in the Northern Hemisphere during the boreal summer, which is supported by the composites of anomalies in the atmospheric circulations and surface energy budget. However, NAO association with CDHW events is relatively weak. The CDHW occurrence over other regions is driven by a combination of these large-scale natural forcing. Our analyses also highlight that the co-occurrence of weekly to sub-monthly scale anomalies in the observed temperature and precipitation may not be always aligned between the observations and the reanalysis. Therefore, caution must be exercised while explaining such observed anomalies on the basis of reanalysis-based circulations and surface energy budget. Overall, our analyses provide a new insight towards concurrent extremes and should help foster research efforts in this area.

Keywords: Compound drought and heatwave | ENSO | PDO | NAO | Mechanistic understanding.

Plain Language Summary

The co-occurrence of drought and heatwave events has increased considerably during the last few decades over many regions of the globe. Therefore, it is imperative to develop an understanding of the factors that influence their regional occurrences. In this study, using a Poisson Generalized Linear Model framework, we identify major regional drivers that are associated with the occurrences of compound drought and heatwave events. Our results show that seasonal occurrences of these compound extremes over many regions in the Southern Hemisphere is associated with the positive phase of ENSO while negative phase of PDO influences their occurrences in the Western North America. Such occurrences in other regions exhibit influence of more than one mode of natural variability. The associations of ENSO and PDO with compound drought and heatwave events can be explained in terms of atmospheric circulations and surface energy budget anomalies.

1. INTRODUCTION

Recent decades have witnessed a notable increase in the concurrence of severe drought and heatwave events in many regions across the globe (Betts et al., 1996; Hao et al., 2013; Mazdiyasni & AghaKouchak, 2015; Seneviratne et al., 2010; Whan et al., 2015; Zscheischler et al., 2018). Such a spatiotemporal coexistence of these extremes is commonly known as a "compound events" (Leonard et al., 2014), which has major implications for social-ecological systems such, as a reduction in crop yields (Ciais et al., 2005; Feng et al., 2019; V. Mishra et al., 2020; Wegren, 2011; Zampieri et al., 2017), an increase in wildfires (Yoon et al., 2015) enhanced tree mortality (Allen et al., 2010), and an exacerbation of human health hazards (Poumadère et al., 2005).

The occurrence of compound drought and heatwave (hereafter CDHW) events may be triggered by a variety of mechanisms ranging from local land-atmospheric feedback loops (Miralles et al., 2019; Santanello et al., 2017) to persistent large-scale ocean-atmosphere circulations anomalies (Hao et al., 2018; Seneviratne et al., 2012). The geographical regions under the influence of such extremes are characterized by prolonged clear skies and a lack of moisture in the lower atmosphere. The deficit in moisture results in the cessation of evaporative cooling, thereby limiting the latent heat fluxes over the land surface (Berg et al., 2014). Subsequently, any further increase in diabatic heating in the region goes directly into increasing sensible heat fluxes and hence exacerbating pre-existing hot and dry conditions (Stéfanon et al., 2014). These anomalies in surface energy budget are often associated with atmospheric blocking and persistent lower-level divergent wind anomalies, which inhibit moisture convergence and lead to prolonged drier surface conditions, provides ample time for a heatwave to develop and intensify over the region (Dong et al., 2018). Many large-scale climate variabilities, including

the El Niño Southern Oscillation (ENSO) (McPhaden et al., 2006), Pacific Decadal Oscillation (PDO) (Newman et al., 2016), and North Atlantic Oscillation (NAO) (Hurrell et al., 2001), are known to have a role in the formation of such high-pressure regimes or stationary blocking zones. Therefore, local-scale climate variability alone may not be able to effectively explain the occurrence of such events (Pepler et al., 2018).

It is shown that large-scale climate oscillations, such as ENSO, play a significant role in the summertime occurrences of compound dry and hot events in tropical regions, particularly over Northern South America, Central and Southern Africa, Southeastern Asia, and Australia (Hao et al., 2018). In addition, a few regional studies have investigated the relationship between compound dry and hot events and the ocean-atmosphere circulation anomalies (Wu et al., 2019) with an aim to develop statistical models for improvement in the predictability of such events (Hao et al., 2019; Hao, Hao, Singh, Xia, et al., 2018; A. K. Mishra & Singh, 2011). However, the calculation of drought (or dryness) index in these previous studies is either based on the monthly precipitation anomalies or on the Standardized Precipitation Index (SPI) (McKee et al., 1993). It is well established that drought quantification using only precipitation while ignoring the impact of temperature may lead to an underestimation of drying (Dai & Zhao, 2017; Mukherjee et al., 2018). Therefore, the use of only precipitation-based indices has the potential to induce considerable methodological uncertainties, which may lead to unreliable estimates of CDHW characteristics. Furthermore, understanding the soil water properties during a hydrological cycle is relevant to the current physical understanding (of feedback processes) of the occurrence of CDHW events over a region (Hao et al., 2018; Mishra & Singh, 2010). Therefore, the use of energy budget methods, which consider soil water as a variable in addition to precipitation and temperature in the identification of CDHW events can be more meaningful in the analysis of

such compound occurrences. In addition, drought and heatwave events are interconnected due to the role of temperature as a common factor in triggering such events. While one of the earlier studies incorporates soil moisture anomalies in the estimation of drying (Hao et al., 2018), it makes use of monthly temperature anomalies in the estimation of CDHW characteristics, potentially compromising the valuable sub-monthly information needed to accurately identify the characteristics of heatwave events. The evaluation of CDHW at a monthly time scale may provide unreliable results as the heatwave events evolve over a period of days to a week. Therefore, in this study, we utilize an integrated temporal framework by incorporating droughts at a weekly time scale, and the heatwaves at a daily timescale to investigate the occurrence of CDHW events on a global scale.

While a plethora of drought indices are available in the scientific literature, the self-calibrated Palmer Drought Severity Index (sc_PDSI) (Wells et al., 2004) incorporates most of the hydroclimatic variables that exert critical controls on the drought characteristics (A. K. Mishra & Singh, 2010; Mukherjee et al., 2018). Given the deficiencies in the earlier studies, we make use of daily observations and an empirical methodology to estimate the frequency of CDHW events for the entire globe. Therefore, our methodology utilizes the weekly self-calibrated Palmer Drought Severity Index (scPDSI) (Wells et al., 2004) for drought, and daily-scale heatwave events.

Our study focuses on each season (DJF, MAM, JJA, and SON) and on the 26 climate regions of the globe (as shown in Figure S1), which are defined in the AR5-SREX (IPCC SREX 2012). Overall, this study aims at providing a mechanistic understanding of the association between the seasonal occurrences of CDHW events and the major modes of climate variability (ENSO, NAO, and PDO) across these climate regions. Here, we quantify such associations based

on a grid-based Poisson Generalized Linear Model (GLM), popularly used to model count data in climate science (Mallakpour & Villarini, 2016; Villarini et al., 2010; Walz et al., 2018). To achieve this objective, we (a) first select the large-scale climate indices as potential drivers for each climate region that influence the regional temperature and precipitation variability during each season by applying a non-parametric partial correlation technique; then (b) later use them as the explanatory variables to form candidate models that are subsequently applied to derive the grid-based GLM focusing on each season, separately; and (c) finally focus on the mechanistic understanding behind such associations by performing a composite analysis based on the relevant atmospheric and surface energy variables. It is important to note that reanalysis datasets are often used to provide mechanistic evidence supporting variations in the observations (precipitation and temperature). However, daily to weekly scale variations, such as CHDW events, in reanalysis may not align perfectly with the corresponding variations in the observations, which may result in inconsistencies when observed variations are explained in terms of anomalies in the reanalysis-based variables. Therefore, in our analyses, we make use of precipitation and temperature both from reanalysis and observations to highlight the inconsistencies that may arise due to this issue.

The paper is structured as follows. In Section. 2.1, we describe the datasets used in the study. Section 2.2 describes the methodology applied in the computation of CDHW events. The initial selection of potential drivers influencing the temporal variability of precipitation and temperature and final best model selection based on Poisson GLM are explained in Section 2.3. Section 3 provides results and discussion, followed by conclusion in Section 4.

2. METHODS

2.1. Datasets

For this study, we select 1982 to 2016 as the analysis period. A daily observed precipitation dataset is obtained from the Global Precipitation Climatology Center (GPCC; https://opendata.dwd.de/climate_environment/GPCC/html/fulldata-daily_v2018_doi_download.html) at 1° horizontal grid spacing (Schamm et al., 2015; Ziese et al., 2018). We select GPCC precipitation because it is fairly consistent in capturing precipitation patterns across different parts of the globe (Sun et al., 2018).

Available water content (AWC) is retrieved from the global database of texture derived AWC (*Webb et al., 2000*), available at 1° horizontal grid spacing. When integrated with the World Soil Data File (*Zobler, 1986*), the resulting dataset captures the soil properties relevant for determining the water storage in the individual soil horizons and for explaining the soil-atmosphere coupling in the lower atmosphere.

The daily observed maximum and minimum temperature (*Tmax*, and *Tmin*) data are obtained from the Climate Prediction Center (CPC). The CPC global temperature data is provided by the National Oceanic and Atmospheric Administration (NOAA) Earth System Research Laboratory's Physical Sciences Division (PSD) (*https://www.esrl.noaa.gov/psd/)* at 0.5° horizontal grid spacing.

Monthly values of ENSO (Nino3.4), NAO, and PDO indices are retrieved from the NOAA Climate Prediction Centre (NOAA CPC; *http://www.cpc.ncep.noaa.gov/*). For the analysis of land-atmospheric dynamics, upper level (200 mb) zonal and meridional wind field, surface latent heat flux (SHF), and surface sensible heat flux (SHF) are obtained from the European Centre for Medium-Range Weather Forecasts Reanalysis 5 (ERA5; *https://cds.climate.copernicus.eu/cdsapp#!/home*). Additionally, we also make use of daily precipitation, *Tmax* and *Tmin* data from the ERA5 to investigate data related inconsistencies. We

apply the Synergraphic Mapping System (SYMAP), described in Maurer et al., 2002, to regrid all dataset at 1° GPCC precipitation grid.

2.2. Frequency of CDHW Events

We define a CDHW event as a heatwave event occurring within the period of an extreme drought event. In this study, at each grid point, a heatwave event corresponds to three or more consecutive days with daily *Tmax* above a threshold (Guerreiro et al., 2018; S. E. Perkins et al., 2012). We calculate unique threshold for each grid point as the 90^{th} percentile of daily *Tmax* using the extended summer seasons (May to October in the Northern Hemisphere, and November to April in the Southern Hemisphere) of the study period. Drought conditions are based on the weekly sc_PDSI following Wells et al., (2004), which considers weekly total precipitation, weekly mean temperature (average of *Tmax*, and *Tmin*), and AWC in the energy-budget framework. A week is considered under extreme drought if the sc_PDSI for that week falls within the bottom ten percent of the sc_PDSI values (= extreme drought threshold) during the study period.

A CDHW event occurs when daily *Tmax* during an extreme drought event exceeds the 90^{th} percentile threshold for three or more consecutive days. The time-series of CDHW events thus obtained are stratified based on four different seasons (DJF, MAM, JJA, and SON). Following the CHDW identifictaion criteria, Figure 1a depicts the time-series of the daily *Tmax* and weekly sc_PDSI for the whole period of the study at a single grid point, and Figure 1b illustrates three instances when a CDHW event takes place in 2012 JJA at the same location. The yearly total number of participating days (frequency) in the CDHW events during a season is considered as the yearly CDHW frequency (CDHWF) for that season. The spatial distribution of

the yearly frequency of extreme drought, heatwave, and the CDHW events observed during all four seasons are illustrated in Figure S2, Figure S3 and Figure S4, respectively. For these and subsequent calculations, we perform separate analyses based on precipitation and temperature from the observations (GPCC and CPCC) and the reanalysis (ERA5). The yearly total number of participating days (frequency) in CDHW events during a season is considered as the yearly CDHW frequency for that season. The spatial distribution of the yearly frequency of extreme drought, heatwave, and CDHW events observed during all four seasons are illustrated in Figure S2, Figure S3 and Figure S4, respectively.

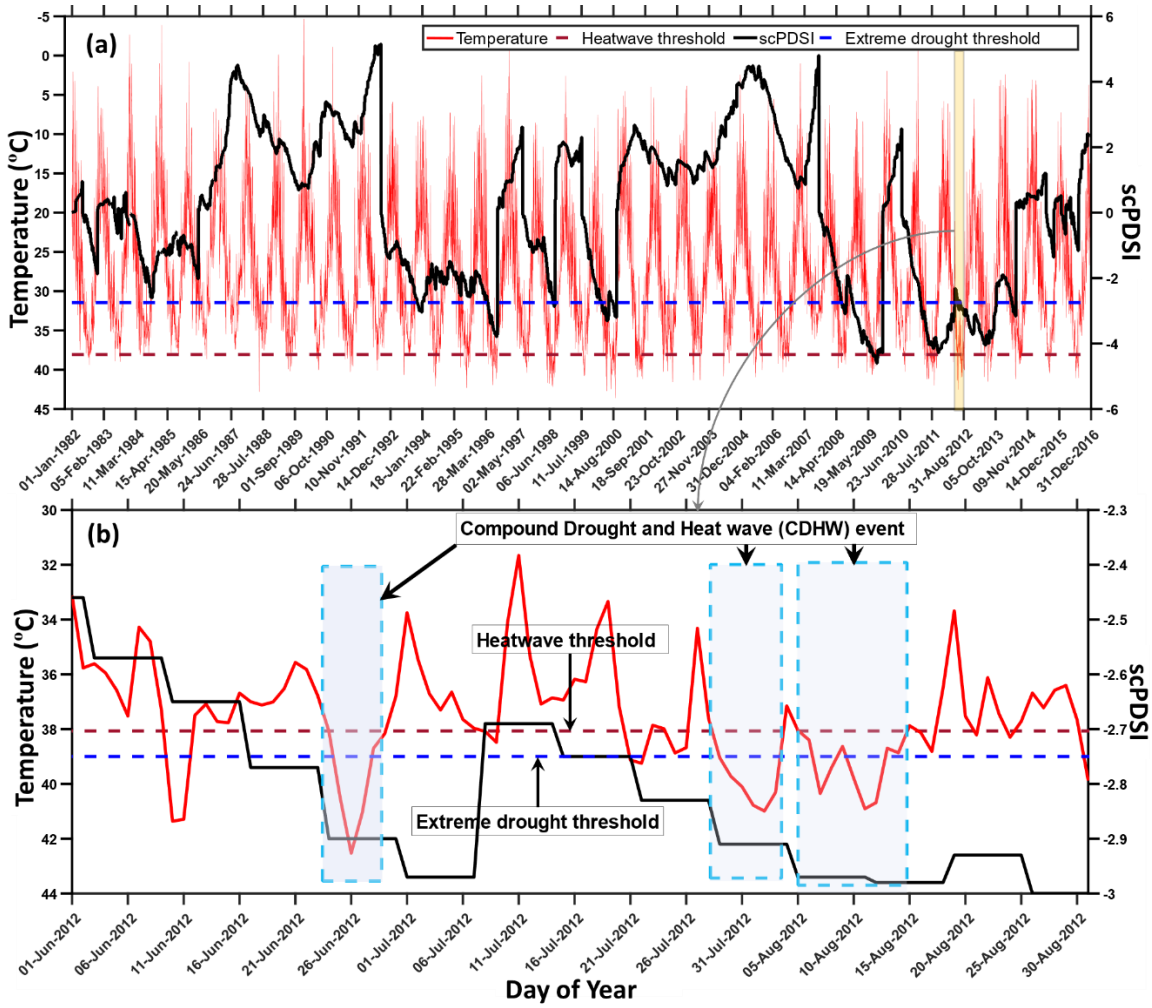

Figure 1. (a) Time series of weekly sc_PDSI and daily *Tmax* based on the GPCC and CPC dataset for the whole period of analysis, 1982 to 2016, for a single grid cell (longitude= -100.5 ,

and latitude = 29.5 (in degrees)), and (b) CDHW events (enclosed within the shaded boxes) for the same grid cell during JJA in the year 2012 (shaded region in (a)). The right y-axis represents the sc_PDSI values and the left y-axis represents the *Tmax*.

2.3. Association between the large-scale climate variability and the occurrence of CDHW events

As previously described, we select three major large-scale natural climate forcing (ENSO, PDO, and NAO) for this study. ENSO — an oscillation of the ocean-atmosphere system in the tropical Pacific — is one of the most important modes of variability impacting global precipitation and temperature on interannual timescales (Dittus et al., 2018; McPhaden et al., 2006; Trenberth et al., 2002). We use the Nino3.4 index to define ENSO. Similarly, NAO is a dominant mode of climate variability over the Northern Hemisphere that ranges from intra-seasonal to multi-decadal time scales, and exerts influence on the variations in air temperature and precipitation across Europe, the Mediterranean Basin, and parts of North America and Asia especially during winter (Hurrell et al., 2001). Likewise, PDO is an annual pattern of monthly sea surface temperature variability in the North Pacific region (Newman et al., 2016), which is known to have a major influence on precipitation variability over North America and Asia.

Using a grid-based Poisson GLM, we quantify the association between these large scale modes of natural climate variability on the inter-annual variability of CDHW events for each season. We quantify such associations in two stages. First, a preliminary selection of the potential large-scale drivers is made based on the regional climate characteristics (represented as regional drivers (RDs), section 2.3.1.). Second, the selected RDs are used as guidelines to identify final predictors for developing the Poisson GLM (section 2.3.2.). The entire methodology employed in the selection of RDs and finally the GLMs for a specific climate region is shown as a flow diagram in Figure 2. A similar technique undertaking the preliminary

selection of possible drivers has been employed in a previous study related to the association between climate variability and regional heatwave event characteristics (Sarah E. Perkins et al., 2015).

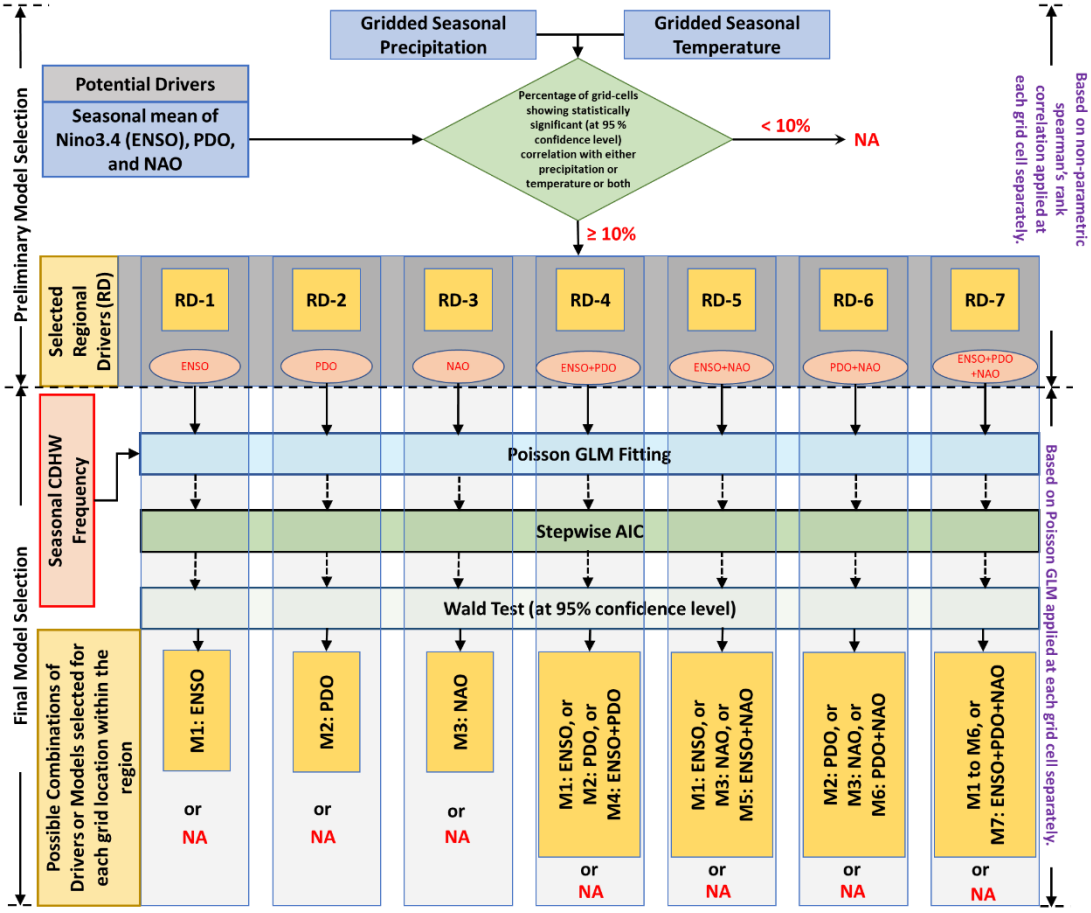

Figure 2 Flow diagram explaining the multi-stage exploration of model selection performed for a specific climate region. "NA" indicates none of the drivers are selected for the region or for any grid cell within the region.

2.3.1. Preliminary selection of potential large-scale drivers

The large-scale climate drivers are selected based on their potential influence on the seasonal precipitation and temperature variability over different geographical regions by using following steps:

(a) First, using non-parametric spearman's rank correlation, we identify possible RDs that influence interannual precipitation and temperature variability at a seasonal time-scale. Monthly precipitation, temperature, and three large-scale climate indices (Nino3.4, PDO, and NAO) are seasonally averaged over the 1982 to 2016 period. Subsequently, correlations between the yearly values of the indices and the meteorological variables are estimated for each season at each grid point. In order to account for the inter-dependence of different climate modes (Meyers et al., 2007; Sarah E. Perkins et al., 2015), we employ partial correlation technique (equation 8) to isolate the influence of individual forcing,

$$r_{xyz} = \frac{r_{xy} - r_{xz} r_{yz}}{\sqrt{(1 - r_{xz}^2)(1 - r_{yz}^2)}} \qquad (8)$$

where r_{xyz} is the relative correlation between *x* (precipitation or temperature), and *y* (ENSO or NAO or PDO) with the effect of z, either of the other indices are removed.

(b) Second, for each climate region, we estimate the percentage of grids where correlations are statistically significant at 95% confidence level, irrespective of the sign of r_{xyz}. If the percentage of grids with significant correlation exceeds 10% of the climate region for either of the two variables, the corresponding RDs are selected as potential forcing factors influencing CDHW events in that region (as *discussed in result, Section 3.1.).*

2.3.2. Poisson Generalized Linear Model (GLM)

The selected RDs for a climate region are used as initial predictors in the Poisson GLM with CDHW events as a predictand. The Poisson GLM is a special form of the generalized linear model (Lindsey, 2000) that is very useful for modeling count data. A general approach is to assume that a random variable N_t follows a non-homogenous Poisson distribution with time-varying rate λ_t, $N_t = Pois(\lambda_t)$, if N_t takes on the values n = 0,1,2,.., with probability

$$P(N_t = n \mid \lambda_t) = \frac{e^{-\lambda_t}\lambda_t^{n}}{n!}. \quad (9)$$

Here, N_t represents the frequency of CDHW events (in days) at each grid during any given season for year t and λ_t is the expected value of Poisson distribution that can be modeled as a function of predictors under the GLM framework as following (McCullagh & Nelder, 1989):

$$\log(\lambda_t) = \beta_0 + \sum_{i=1}^{k} \beta_i x_i(t), \quad (10)$$

$x_i(t)$ represents selected large-scale drivers, k is the number of predictors, and β_i represents the coefficients for the respective predictors. In order to account for areal variations at different latitudes, we modify Eq. (10) as following:

$$\log(\lambda_t) = \beta_0 + \sum_{i=1}^{k} \beta_i x_i(t) + \log(\cos\phi). \quad (11)$$

where ϕ is the latitude and $\log\cos\phi$ serves as an offset term with coefficient 1.

We obtain coefficients for the respective predictors in Eq. (11) by maximizing the log-likelihood function for the Poisson GLM defined as,

$$L = \sum_{t=1}^{T} N_t \log\lambda_t - \lambda_t - \log(N_t!), \quad (12)$$

The maximized log-likelihood (L) provides an indirect measure of how well the model fits the data. However, a positive bias in the estimates of L amplifies as the number of predictors increase, resulting in overfitting of the model. Such a situation can be avoided by using Akaike Information Criteria (AIC) that accounts for these biases and removes redundant predictors to prevent overfitting. The initial predictors are subjected to a stepwise regression approach based on the AIC estimated as,

$$AIC = 2p - 2\ln L \quad (13)$$

290 where p is the number of parameters in the model.

291 The Poisson GLM that has the smallest AIC value is considered as the best model for that
292 location. However, the AIC score does not provide any evidence about the absolute quality of the
293 model. Therefore, the chosen predictors of the best AIC model are further tested for statistical
294 significance based on the Wald test. Only predictors, significant at 95% confidence level, are
295 included in the final Poisson GLM to compute the regression coefficients at each grid location.

296 In order to determine the significance of relationship between the estimated regression
297 coefficients β_i and the random variable N_t, we test the null hypothesis that $\beta_i = 0$ is true based
298 on the test statistic Z. In other words, we assume that the expectation of the fitted regression
299 coefficient $\hat{\beta}$ is 0. Upon standardizing the regression coefficient of individual predictors, we
300 obtain the test statistic Z, which follows a normal distribution as following (Casella & Berger,
301 2002):

302 $$Z = \frac{\hat{\beta} - 0}{\hat{\sigma}_{\hat{\beta}}} = \frac{\hat{\beta}}{\hat{\sigma}_{\hat{\beta}}}. \quad (14)$$

303 The test statistic Z allows test against a two-sided alternative hypothesis that $\beta_i \neq 0$ at a
304 significance level of $\alpha = 0.05$ in which the critical value is the upper $\alpha/2$ percentage point of the
305 standard normal distribution, $z_{\alpha/2}$. The regression coefficient is considered to be statistically
306 significant if $|Z| \geq z_{\alpha/2}$, thereby, rejecting the null hypothesis that $\beta_i = 0$.

307 **3. Results and Discussion**

308 *3.1. Potential regional drivers at seasonal scale*

309 The spatial maps of seasonal partial correlations, corresponding to ENSO, PDO, and
310 NAO, are shown in Figures S5 to S7 for the observed precipitation and temperature and in

311 Figures S12 to S14 for the reanalysis precipitation and temperature. These correlations become
312 the basis of our predictor selection in the Poisson GLM model. Correspondingly, the percent of
313 total grid points within each region where the correlations are statistically significant is shown as
314 bar plots in Figures S8 to S11 for observations, and in Figure S15 to S18 for reanalysis. The use
315 of 10% of the total grid points within a region as a minimum criterion for the selection of RDs as
316 predictor leads to a total seven combinations (Figure 2). The geographical distribution of these 7
317 RDs is shown in Figure 3.

318 If we consider similarities between the left column (observations) and the right column
319 (reanalysis) RDs, then precipitation and temperature variations are influenced by PDO and NAO
320 (RD6) over Northern Europe and Asia (Figure 3a-3b) in DJF, Eastern Asia and Sahara and
321 Central America in JJA, and Eastern America, Canada and Northern Europe in SON. Similarly,
322 ENSO exhibits a substantial footprint in the monsoon regions, including Southern South
323 America, Northern Australia and South Africa in DJF, and most of South America, South Asia
324 and Northern Australia in SON, consistent with the earlier finding (Wang et al., 2017). PDO
325 (RD2) also exhibits influence over many regions of Asia in SON while all of them (ENSO, PDO,
326 NAO; RD7) seem to have an influence over South Asia, Southeast Asia, Northern Australia and
327 Western Asia, which is consistent with previous findings (Rajagopalan et al., 2000; Sun et al.,
328 2016; Xiao et al., 2015). The interaction of PDO with NAO, and ENSO in influencing the
329 precipitation and temperature variability has been reported in the previous studies (Ding et al.,
330 2017; Knippertz et al., 2003).

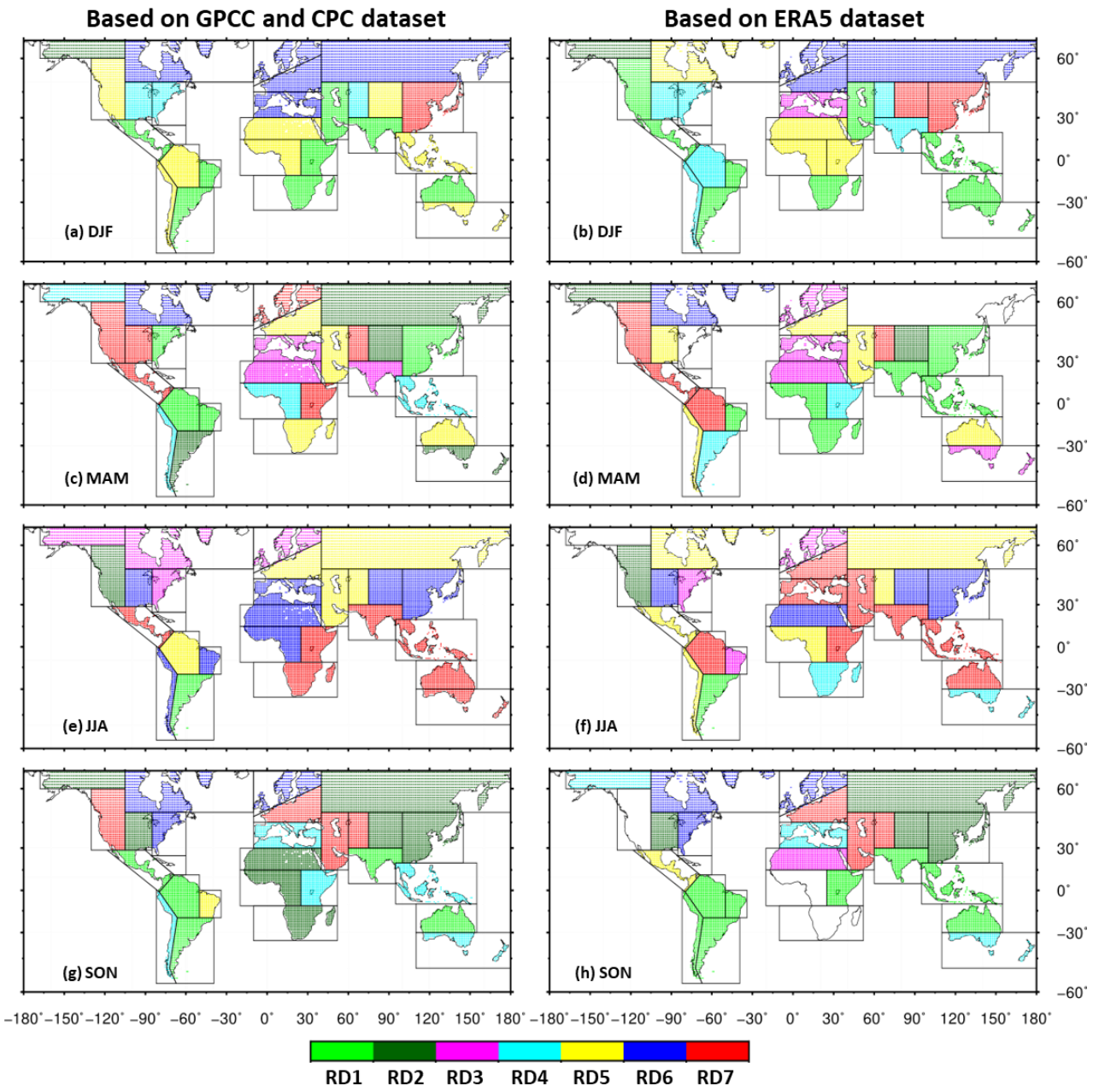

Figure 3 Regional Map showing combinations of potential regional drivers (RD1 to RD7; filled circles) for the 26 AR5-Climate regions based on the GPCC and CPC (left panel), and the ERA5 (right panel). The list of large-scale climate variabilities corresponding to each of the selected combinations of regional drivers (RD1 to RD7) is provided in Figure 2.

The existence of several differences between the left and right columns in Figure 3 highlight the fact that the identification of regional drivers of precipitation and temperature variability depends on the source of data. For instance, RDs based on observations show the influence of PDO, and NAO (RD6) over Canada and Mediterranean in DJF (Figure 3a) while use of ERA5 reanalysis replaces PDO with ENSO (RD5) over Canada and only shows the influence of NAO (RD3) over Mediterranean . Similarly, unlike observations, reanalysis doesn't exhibit influence of PDO over Western and Southern Africa in SON, and over Northern Asia in MAM. Inconsistencies also exists in many other regions and seasons (Figure 3).

The best AIC models that are also statistically significant at the 5% significance level, which are obtained by fitting the RDs (Figure 3) as explanatory variables in the Poisson GLM, are presented geographically in Figure 4. It should be noted that the final models over a region can be identical to the RDs, a subset of RDs or none, which is explained in Figure 2. For instance, Northern Asia that has RD5 (ENSO and NAO) as the selected combination of regional drivers (Figure 3e, 3f) in JJA shows M1 (ENSO), M3 (NAO), and M5 (ENSO, NAO) as the best fitted models (Figure 4e, 4f) after the application of the AIC and Wald tests. Similarly, Eastern Asia that has RD2 (PDO) as the selected regional driver (Figure 3 g, h) in SON has no best fitted model (Figure 4g, 4h) after the application of the AIC and Wald tests. Moreover, as previously noted, choice of data source also influences the RDs and hence the final best fitted models (Figure 4, left column versus right column). We identify such regions and hereafter highlight them with a bold boundary.

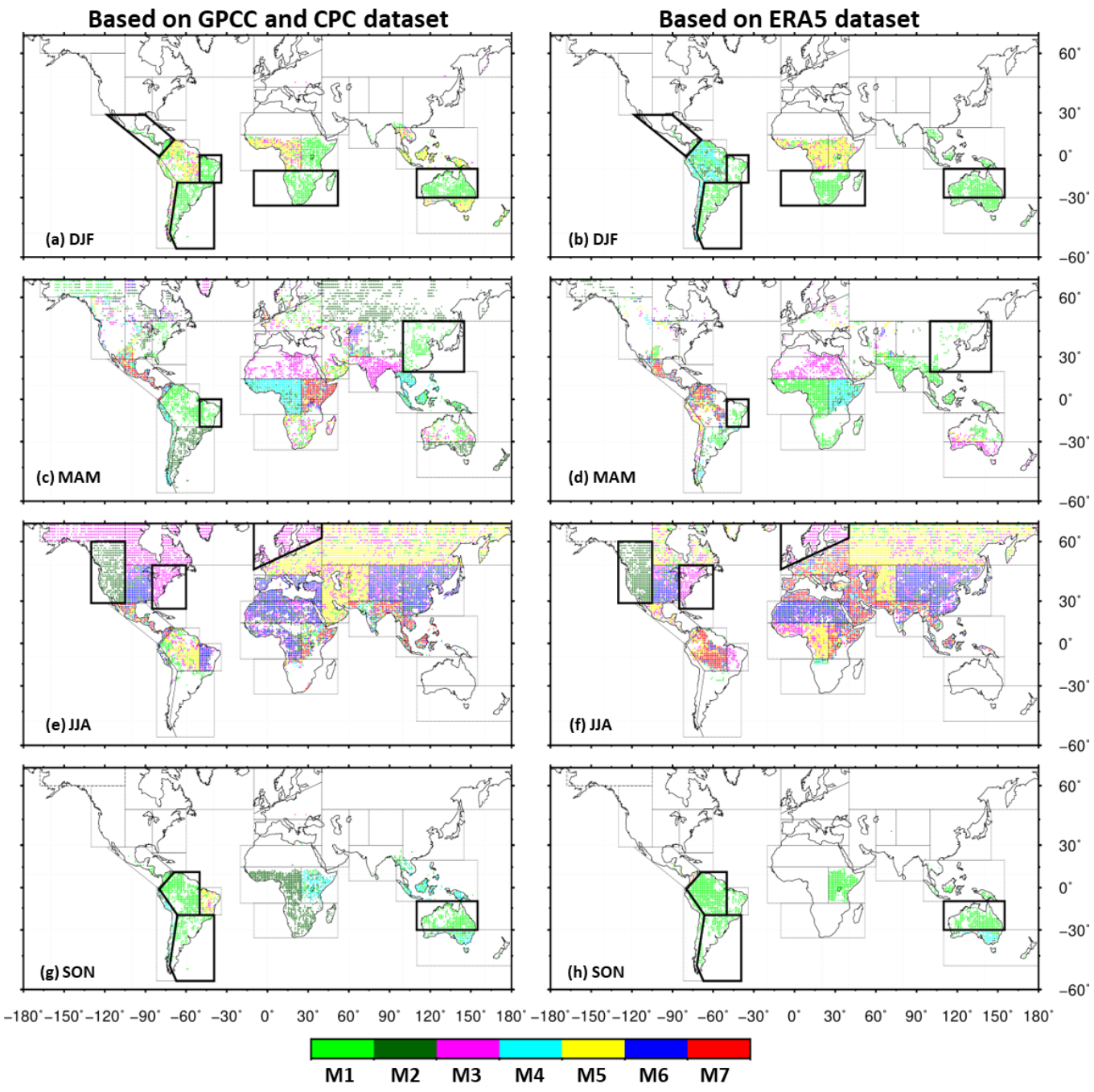

356

357 **Figure 4** Spatial map of the best models (M1 to M7; filled circles) explaining the inter-annual
358 variability of CDHW events from 1982 to 2016 based on the GPCC and CPC (left panel) , and
359 the ERA5 (right panel), which are identified by the Poisson GLM. The list of large-scale natural
360 climate forcing corresponding to each of the selected models (M1 to M7) is provided in Figure 2.

The bold boundaries indicate regions exhibiting the influence of a single large-scale driver, which is also consistent in both datasets.

3.2. Relationship between CDHW events and large-scale climate variability

The formulation of Poisson GLM indicates that the estimated coefficients can be interpreted as a direct measure of sensitivities (Mallakpour & Villarini, 2016; Villarini et al., 2010; Walz et al., 2018). In addition, the logarithmic function applied in the Poisson GLM is useful to determine the relative importance of every selected large-scale driver, such that 1 unit increase in the regression coefficient (β_i) can lead to a $\exp(\beta_i + 1)$ times impact on the predictand. Thus, the higher magnitude of the regression coefficient corresponds to the higher relative impact of the associated driver. Positive (negative) values of the regression coefficients imply that the warm (cold) phase of the associated large-scale drivers has a positive (negative) association with the CDHW events. In this section, we discuss the impacts of warm and cold phases of the associated large-scale drivers across different climate regions of the globe.

3.2.1 El-Nino Southern Oscillation (ENSO)

Figure 5 shows grid points with statistically significant Poisson GLM regression coefficients corresponding to ENSO and CDHW events. Given the dependence of RDs and resulting final models on the choice of data, we only focus on those regions where the results are consistent between observations (left column) and reanalysis (right column). A significant positive influence of the warm phase of ENSO (El Niño) exists in the Southern Hemisphere during the austral summer months (DJF; Figure 5a) over the Amazon, Southern Africa and Northern Australia, and during SON over the Southern Australia. Some of these associations are consistent with earlier studies (Hao et. al., 2018; Hirons & Klingaman, 2015; Min et al., 2013). The negative

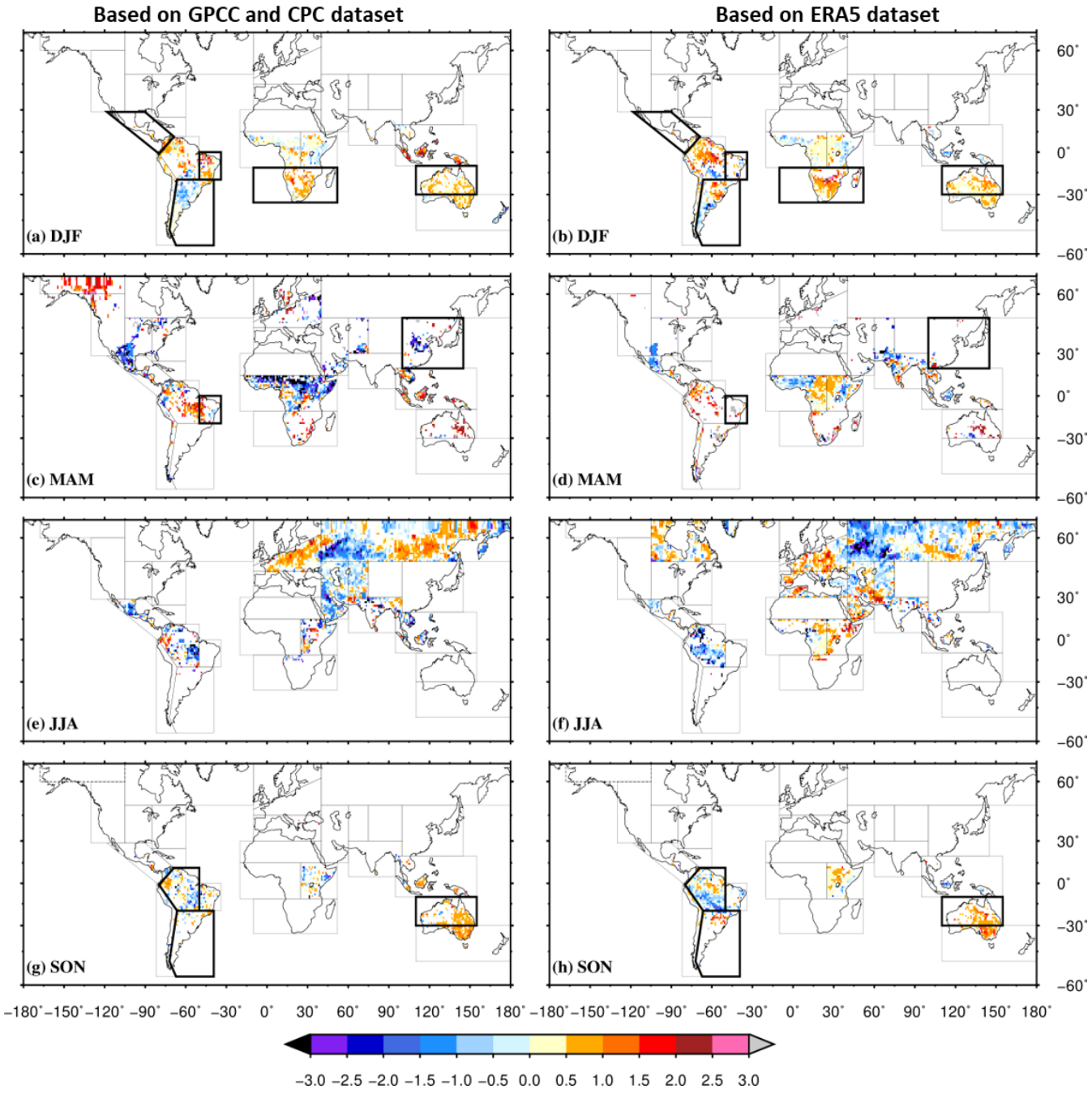

384

385 **Figure 5** The statistically significant Poisson GLM regression coefficients for ENSO (Nino3.4)
386 based on the GPCC and CPC dataset (left column), and the ERA5 (right column), explaining the
387 interannual variability of CDHW events during (a, b) DJF, (c, d) MAM, (e, f) JJA, and (g, h)
388 SON. The bold boundaries indicate regions exhibiting the influence of a single large-scale driver,
389 which is also consistent in both datasets.

phase of ENSO (La Niña) exhibits a significant positive influence over parts of Asia in JJA and over the parts of Central America and Western Africa in MAM. Central Europe also exhibits positive influence of El Niño in JJA. However, ENSO is not the only driver over these regions during JJA. Unfortunately, several regions exhibit inconsistences between the observations and reanalysis, including Southeast Asia during all the four seasons; Alaska, Eastern and Western Africa, and parts of Southern South America in MAM; Canada, and West Asia in JJA, and East Africa in SON.

3.2.2 Pacific Decadal Oscillation (PDO)

The Poisson GLM regression coefficients for PDO explaining the interannual variability of CDHW events during all four seasons is presented in Figure 6. With the exception of JJA, all other seasons exhibit inconsistency in the influence of PDO. In JJA, negative phase of PDO is the sole driver over Western North America (highlighted by bold boundary in Figure 6) and is one of the drivers over central North America, Sahara, Mediterranean, East Asia and Tibet. The role of PDO in modulating the CDHW events over the eastern part of Asia has been previously reported (Yu et al., 2018). Previous studies also suggest that the anomalies over the northeastern and tropical Pacific have a significant impact on the occurrence of CDHW events in the conterminous US (Dulière et al., 2013; Kamae et al., 2017; McCabe et al., 2004; Peterson et al., 2013).

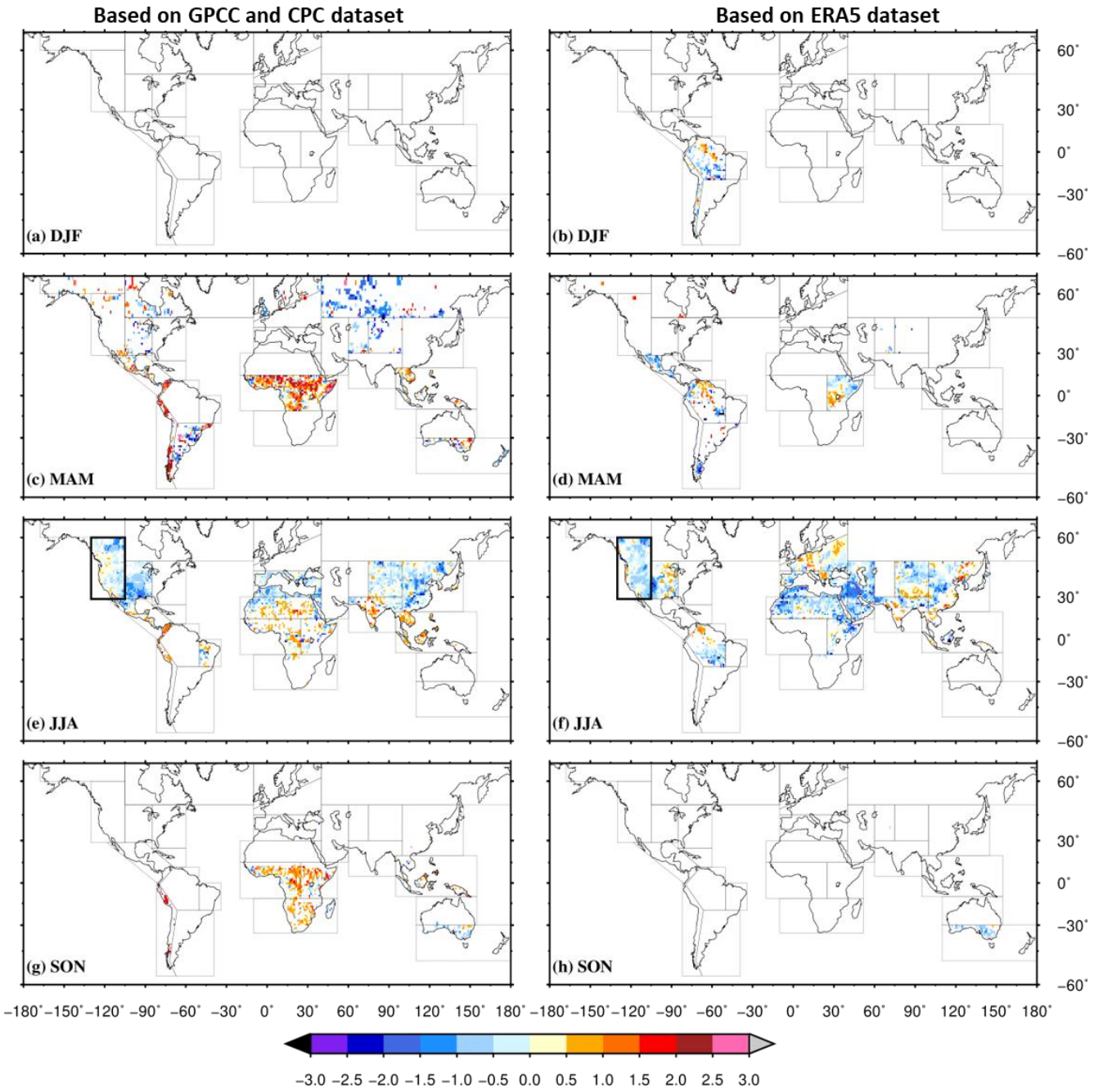

Figure 6 Same as in Figure 5 but for PDO.

3.2.3 North Atlantic Oscillation (NAO)

Figure 7 presents the significant Poisson GLM regression coefficients for NAO during the four seasons. The strength of regression coefficients is relatively weak in the case of NAO. However, unlike ENSO and PDO, the results are generally independent of the data source. Both

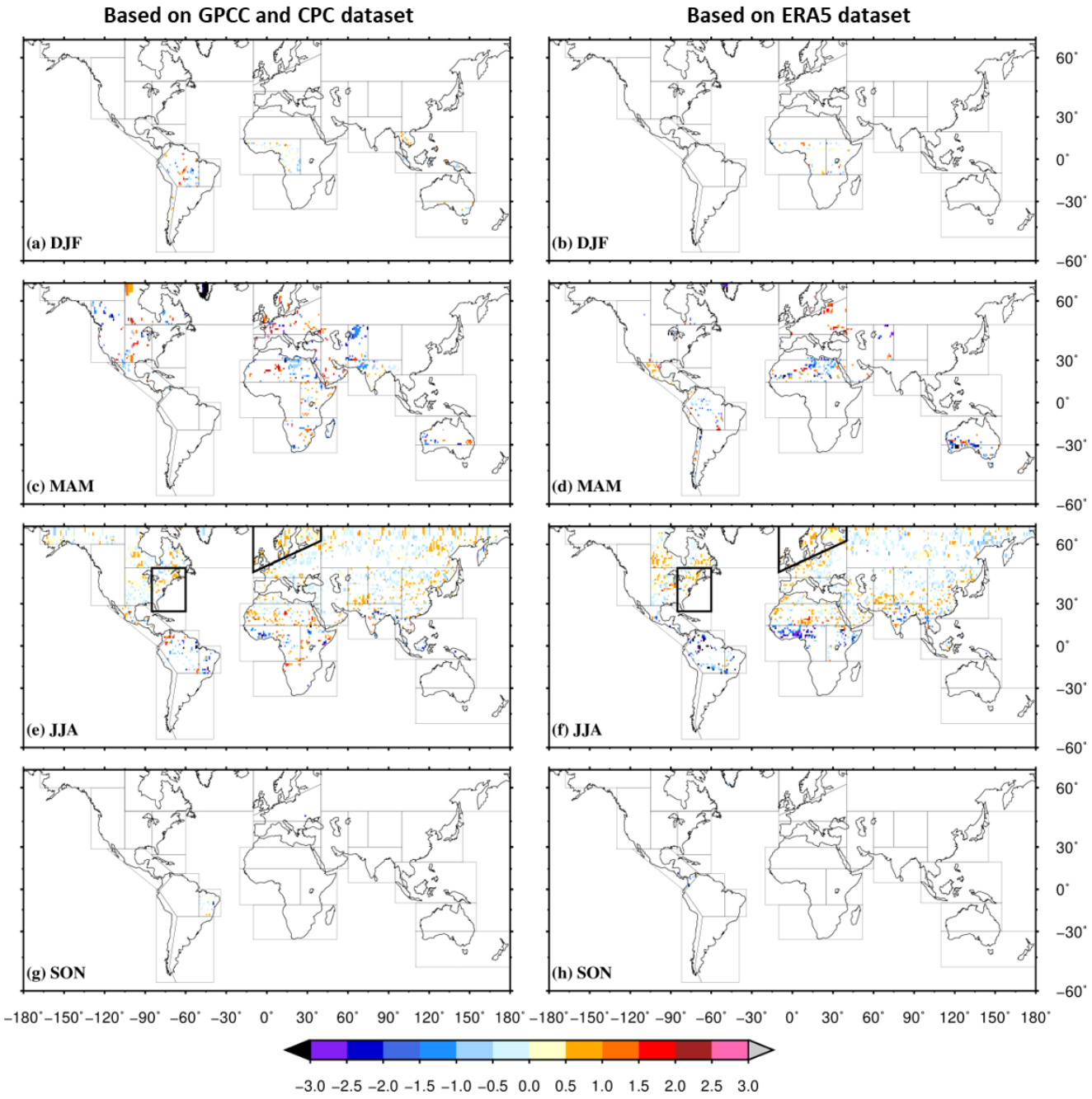

414

415 **Figure 7** Same as in Figure 5 but for NAO.

416

417 datasets show NAO as the sole significant influencer over Northern Europe and Eastern North

418 America (highlighted by bold boundaries in Figure 7) in JJA. Apart from that, in combination

419 with other modes, role of NAO is seen in JJA over most of Asia, Europe, Northern Africa and

Eastern North America. Similarly, negative phase of NAO exhibits more influence over Northern Asia and West Africa while influence of the positive phase of NAO is limited to Northern Europe and parts of Central Asia. Many earlier studies support the influence of NAO on the occurrence of CDHW events over Europe (Cassou et al., 2005) Asia (Filippi et al., 2014) and North America (Mahlstein et al., 2012; Trouet et al., 2018).

3.3. Atmospheric anomalies associated with warm and cold phases

In order to understand atmospheric anomalies associated with the large-scale climate drivers that lead to their regional associations with CHDW events, shown in Figures 5 to 7, we analyze seasonal anomalies in upper-level (200 mb) velocity potential and divergent winds during warm and cold phases of ENSO, PDO, and NAO. Dry and hot conditions are generally associated with lower level divergence (or upper level convergence) anomalies in the atmosphere (Seager et al., 2010; Trenberth et al., 2000). The seasonal analyses of divergent winds illustrate the variations in the Walker and Hadley circulation across seasons (Figure S19). In DJF, upper-level divergent wind centers are in the Southern Hemisphere over the western Pacific, the eastern Indian Ocean and the Amazon, which correspond to lower-level monsoonal flow over these regions. In JJA, divergent winds centers shift to the Northern Hemisphere over the Asian and North American monsoon regions. Anomalies in divergent winds can occur due to sea surface temperature anomalies in various oceanic basins (Ashfaq et al., 2011), which act as a remote connection between natural modes of climate variability and climates over many terrestrial regions.

It should be noted that those regions where more than one large-scale driver influences the occurrence of CDHW events (Figure 3; RD4 to RD7), atmospheric anomalies based on the warm and cold phases of a single driver may not be able to provide a mechanistic explanation of

overlying dynamic causes. Therefore, our explanation of atmospheric anomalies is mostly limited to those regions where a single driver is shown to have an influence (M1 to M3; bold boundaries Figure 4 to 7) in the observations and reanalysis.

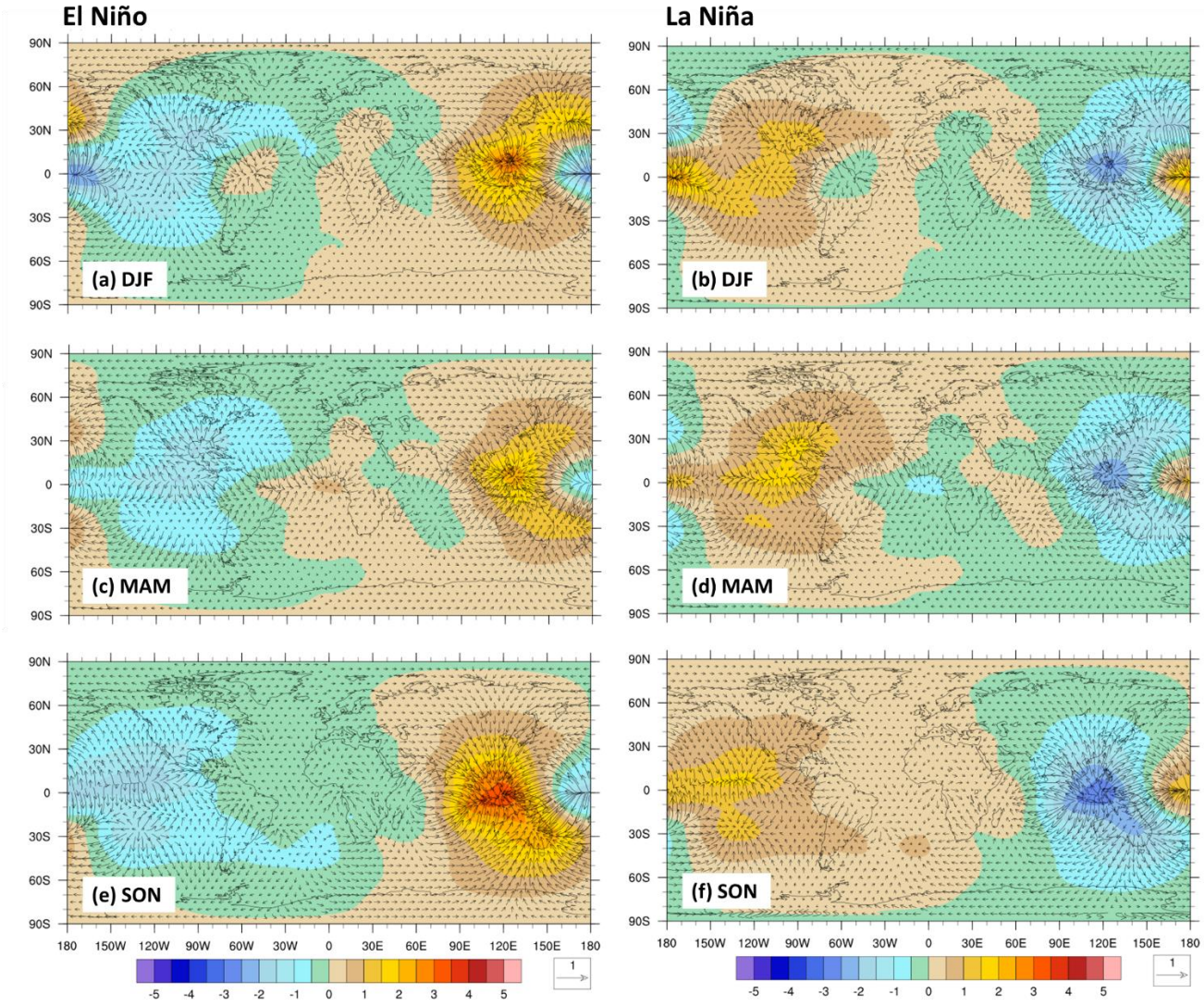

Figure 8 El Nino (left panel) and La Nina (right panel) based anomalies in divergent winds vectors (m/s) and velocity potential (color shading, unit:m^2/s, scaled by 10^6) contours at 200 mb with respect to the climatology during (a-b) DJF, (c-d) MAM, and (e-f) SON.

Figure 8 illustrates seasonal anomaly in the velocity potential and upper-level divergent winds for the El Niño (left panel) and La Niña (right panel) in DJF, MAM, and SON. The robust positive association between El Niño and the CDHW events during DJF (Figure 5a, 5b) is explained by the anomalous upper-level convergence over Amazon, Southern Africa, and Australia (Figure 8a). Similarly, upper-level anomalous convergence is present over Australian continent in SON during El Niño, consistent with the positive association of El Niño and the CDHW events during that season (Figure 5g, 5h)). Given that upper-level convergence is an indicator of lower-level divergence or clear weather conditions, these anomalies favor reduction of moist flow particularly during the austral summer over these regions. Circulation anomalies in JJA during El Niño (La Niña) are also consistent with its association with the JJA CDHW events over Central Europe (Central Asia and parts of Northern Asia) (Figure S20). However, ENSO is not the only driver over these regions.

Similarly, Figure 9 depicts the upper-level circulation anomalies during the warm and cold phases of PDO and NAO in JJA. Western North America is the only region where PDO is the sole driver associated with the occurrence of CDHW events in JJA (Figure 4). The sign of regression coefficient suggests that it is the cold phase of PDO that exhibits positive correlation with CDHW (Figure 6e, 6f). This association is consistent with anomalies in upper-level divergent winds in JJA during the cold phase of PDO, which exhibit anomalous upper-level convergence centered over the eastern Pacific. Moreover, the anomalies in upper-level divergent winds over Central America explain the positive association of the CDHW (Figure 6b) events with the cold phase of PDO in MAM (Figure S21). However, this association is not present in the case of observations based CHDW events (Figure 6).

As previously noted, magnitudes of regression coefficients are substantially weaker for NAO compared to ENSO and PDO (Figure 5-7), which suggest relatively weak influence of NAO in the occurrence of CDHW events. During JJA, when NAO influence is spatially more visible (Figure 7e, 7f), upper-level circulation anomalies are relatively small (Figure 9c, 9d), which are consistent with weak magnitudes of regression coefficients.

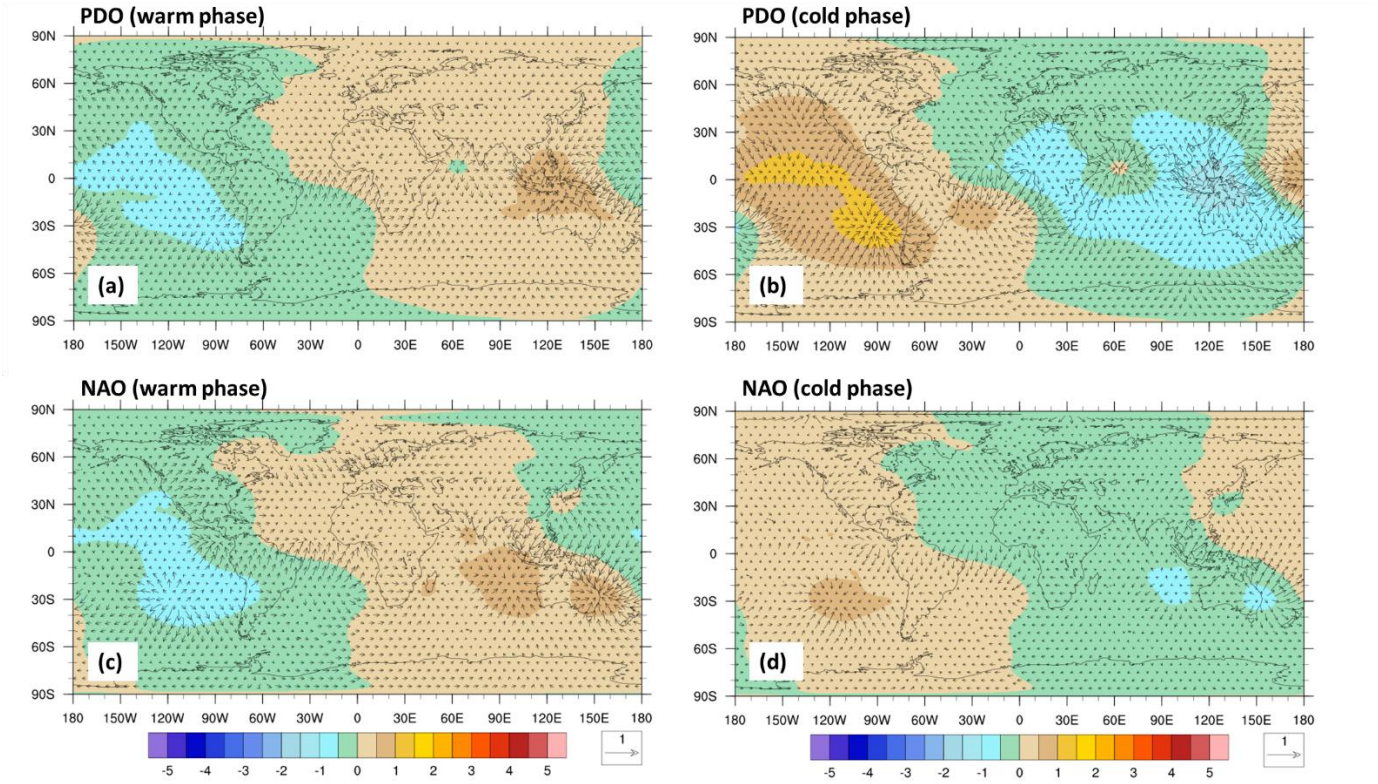

Figure 9 Same as in Figure 8 but based on warm (left panel) and cold (right panel) phase of (a, b) PDO, and (c, d) NAO During the JJA season.

It is also important to highlight that regions where a single large-scale driver only exists in the observations-based analysis, reanalysis-based circulations anomalies do not support such associations (Figures S21, S22). For instance, in SON, only in the analyses based on the observed precipitation and temperature, PDO appears as the single large-scale driver (Figure 3g,

3h) over Western and Southern Africa and positive phase of PDO exhibits association with CDHW events (Figure 4g, 4h). However, anomalies in the reanalysis-based upper-level circulations over Africa exhibit anomalous divergence, which correspond to lower-level convergence or conditions opposite to the ones needed for CDHW events (Figure S21). Likewise, parts of North America and Northern Europe in JJA exhibit NAO as the sole driver in the analyses based on the GPCC and CPC datasets, but ERA5-based circulation anomalies do not support such association of NAO with the occurrence of CDHW events over these regions. These inconsistencies suggest that use of reanalysis to explain anomalies in the observations, particularly those related with fine temporal variations, may not be a robust strategy.

3.4. Surface energy budget anomalies associated with the warm and cold phases

The role of land-atmospheric feedbacks in modulating the characteristics of CDHW events is well recognized over many regions of the globe (Lee et al., 2016; Santanello et al., 2017; Seneviratne et al., 2010; Zhou et al., 2019, 2019). Under dry and warm conditions, the positive land-atmospheric feedback processes, which are also referred to as soil moisture-temperature coupling, are one of the local-scale controlling factors governing surface energy budget. Characterized by the cessation of cooling from evaporation under dry conditions, such positive feedback loops lead to a decrease in the latent heat fluxes (LHF) and an increase in the sensible heat fluxes (SHF). It is well established that natural climate forcing influence terrestrial water availability, soil moisture deficits and evaporation rates through their controls on precipitation generating mechanisms (Martens et al., 2018; Miralles, Berg, et al., 2014; Park et al., 2012). These variations in the terrestrial water cycle directly impact the land-surface energy

feedbacks and hence influence the occurrence of CDHW events (Miralles, Teuling, et al., 2014).

We investigate the influence of ENSO, PDO, and NAO on these land-surface and atmosphere feedbacks by analyzing seasonal anomalies in the SHF and LHF during the warm and cold phases of ENSO, PDO, and NAO with respect to their seasonal climatology (Figure S23). We use a two-sample Student's *t*-test at a 5% significance level to test the significance of anomalies (McDonald, 2009). For any given season, a positive (negative) anomaly in the SHF and a corresponding negative (positive) anomaly in the LHF characterizes a positive land-surface and atmospheric feedback. Thus, the results from the composite analysis are discussed hereafter based on the positive feedback loops with an aim to provide a localized mechanistic explanation behind the association between the large-scale climate forcing and the occurrence of CDHW events, as shown earlier in Figures 5, 6, and 7. As noted earlier, the design of these analyses limits their use only to those cases where a single natural climate forcing is consistently identified as the regional driver in observations and reanalysis.

A significant simultaneous increase in the SHF and decrease in LHF is witnessed over the parts of the Southern Hemisphere in DJF where El Niño exhibits a positive association with the occurrence of CDHW events (Figures 10a, S24) and where upper-level circulation anomalies favor dry conditions on the surface (Figure 8a), such as over Southern Africa and western parts of Northern Australia. Similarly, a significant increase in the SHF and decrease in the LHF is present over major parts of Australia in SON (Figures 10e, S24) that exhibit a positive association between El Niño and CDHW, and upper-level circulation anomalies that favor drying.

In case of the cold phase of PDO, a delayed effect of the positive land-atmospheric feedbacks can be noticed over the Western North America during the JJA season (Figure 10d). Given that

JJA is the dry season over the Western North America, the surface drying in JJA may be in part influenced by the significant positive high SHF and negative LHF anomalies in the preceding season (MAM; Figures 11b, 11d, S25), which is consistent with its positive association with the CDHW events (Figure 6f). However, results are not very clear in the case of NAO over Eastern North America and Northern Europe in JJA, where it is the only large-scale driver in both datasets. This inconclusiveness in the case of NAO is because both phases of NAO appear to have association with CDHW events over these regions in JJA, which is also relatively weak (Figure 7e, 7f).

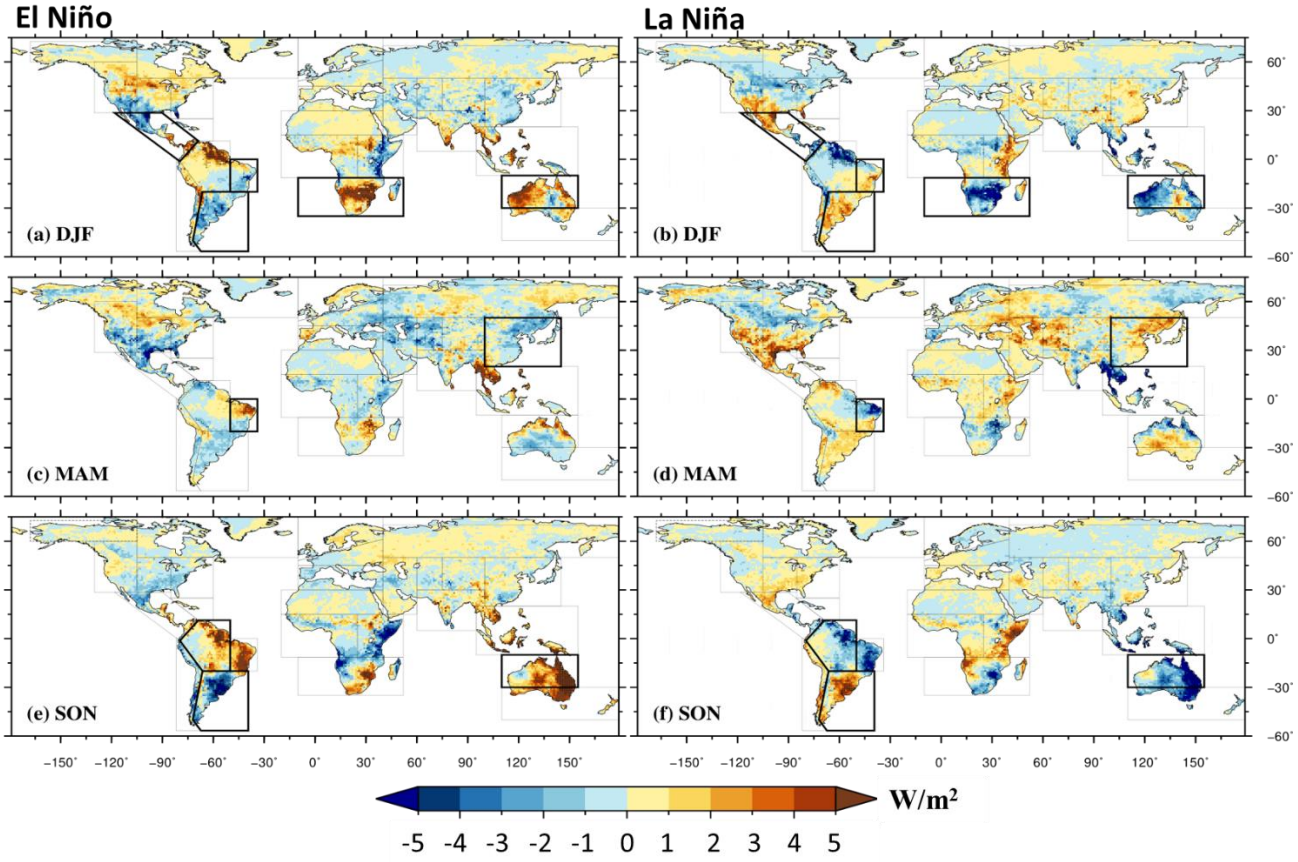

Figure 10 El Nino (left panel) La Nina (right panel) based anomalies in sensible heat flux with respect to the climatology during (a, b) DJF, (c, d) MAM, and (e, f) SON. Stippling represents

544 statistically significant at 95% confidence level. All units are in W/m^2. The sign convention
545 implemented for the fluxes is positive upwards.
546

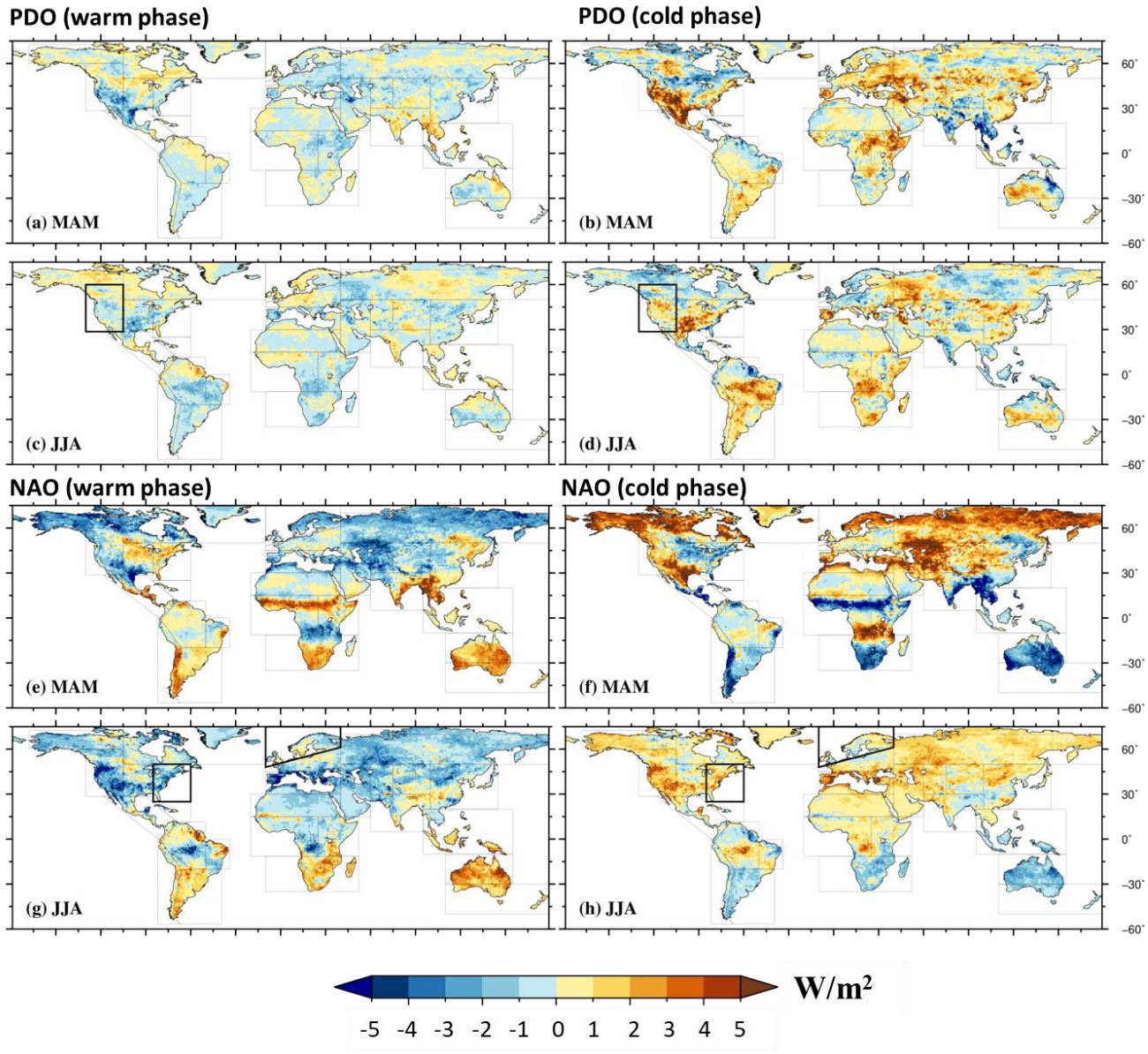

547

548 **Figure 11** Same as in Figure 11 but based on the warm (left panel) and cold (right panel) phase
549 of PDO. All units are in W/m^2. The sign convention implemented for the fluxes is positive
550 upwards.
551

552 Overall, the anomalies in circulation patterns and surface energy fluxes can explain
553 influence of ENSO, NAO, and PDO in the occurrence of CDHW events when any one of them is
554 the only driver in both datasets (indicated by bold boundaries in Figure 5-7). Exceptions in the
555 case of NAO exist, which are understandable given its relatively weak, mixed and spatially
556 sparse relationship with CDHW events (Figure 7). Furthermore, as it is in the case of circulation
557 anomalies, reanalysis-based surface energy fluxes variations are inconsistent when association of
558 ENSO, NAO, and PDO with the CDHW events is only limited to the observations-based
559 analyses (Figure S27).
560
561 4. **Summary and Conclusions**
562 Using weekly sc_PDSI and daily *Tmax*, we estimate the yearly frequency of CDHW
563 events for four seasons from 1982 to 2016 period over the 26 AR5 climate regions of the globe.
564 Moreover, an association between three major large-scale climate forcing (ENSO, PDO, and
565 NAO), and the yearly occurrences of CDHW events is investigated based on the regression
566 coefficients estimated using Poisson GLM for each season. Furthermore, we examine the
567 robustness of such associations by using precipitation and temperature from two sources
568 (observations and reanalysis).
569 Based on the estimates of Poisson regression coefficients, we find that the warm phase of
570 ENSO has a relatively more dominant and robust footprint, specifically over the Southern
571 Hemisphere. ENSO alone has a significant influence on the yearly occurrences of CDHW events
572 over Northern Australia in DJF and SON, over Southern Africa, Southern parts of South
573 America in DJF, and over Amazon in SON. These regions exhibit consistent associations of
574 CHDW events with ENSO in the observation and reanalysis, which are supported by the

anomalies in the reanalysis-based circulations and surface energy fluxes during the respective seasons. Similarly, the cold phase of PDO exhibits positive influence over Western North America in JJA, which is associated with anomalous upper-level convergence and strong surface drying in JJA and preceding season. Our results indicate a weak influence of NAO in the occurrence of the CHDW events.

In this study, we have provided a preliminary mechanistic understanding regarding the association between the major modes of natural climate variability and the occurrence of CDHW events across the globe. However, there are a number of caveats in our methods and analyses that require improvements in future studies. For instance, the frequency of CDHW events depends on the choice of indices for heatwave and drought identification. The identification of heatwaves, in particular, can vary if a different percentile threshold or consecutive days criteria is used. Therefore, further research is needed for more robust definition of compound drought and heatwave events. Similarly, this study only focuses on three modes of natural climate variability and potentially ignores other large-scale forcing such as SST anomalies in the Indian Ocean (Indian Ocean Dipole), Tropical North Atlantic and Equatorial Atlantic (Atlantic Niño) that can independently impact the occurrences of CDHW events or their co-occurrence with ENSO, PDO and NAO can potentially enhance or dampen their impact (Chang et al., 2006; Saji & Yamagata, 2003). Moreover, our analysis also highlights that weekly to sub-monthly scale anomalies in temperature and precipitation, which in some cases give rise to CHDW events, may not be always aligned between the observations and reanalysis across the globe. Therefore, caution must be exercised in the mechanistic explanation of observed anomalies in the precipitation and temperature on the basis of anomalies in the reanalysis-based circulations and surface energy budget. Nonetheless, our analysis provides a new insight into the mechanistic understanding

towards concurrent extremes and should help foster research efforts in this area, especially in improving the seasonal predictability of such extremes.

Acknowledgment

This study was supported by the National Science Foundation (NSF) award # 1653841 in collaboration with Regional and Global Climate Modeling Program within the Office of Science of the US Department of Energy (DOE). We are thankful for the data provided by the NOAA Climate Prediction Centre (NOAA CPC; http://www.cpc.ncep.noaa.gov/), Global Precipitation Climatology Center (GPCC; https://www.dwd.de/EN/ourservices/gpcc/gpcc.html), and high-resolution European Centre for Medium-Range Weather Forecasts Reanalysis 5 (ERA5).

References

Allen, C. D., Macalady, A. K., Chenchouni, H., Bachelet, D., McDowell, N., Vennetier, M., et al. (2010). A global overview of drought and heat-induced tree mortality reveals emerging climate change risks for forests. *Forest Ecology and Management*, *259*(4), 660–684. https://doi.org/10.1016/j.foreco.2009.09.001

Ashfaq, M., Skinner, C. B., & Diffenbaugh, N. S. (2011). Influence of SST biases on future climate change projections. *Climate Dynamics*, *36*(7), 1303–1319. https://doi.org/10.1007/s00382-010-0875-2

Berg, A., Lintner, B. R., Findell, K. L., Malyshev, S., Loikith, P. C., & Gentine, P. (2014). Impact of Soil Moisture–Atmosphere Interactions on Surface Temperature Distribution. *Journal of Climate*, *27*(21), 7976–7993. https://doi.org/10.1175/JCLI-D-13-00591.1

Betts, A. K., Ball, J. H., Beljaars, A. C. M., Miller, M. J., & Viterbo, P. A. (1996). The land surface-atmosphere interaction: A review based on observational and global modeling perspectives.

624 *Journal of Geophysical Research: Atmospheres*, *101*(D3), 7209–7225.
625 https://doi.org/10.1029/95JD02135
626 Casella, G., & Berger, R. L. (2002). *Statistical inference* (2nd ed). Australia ; Pacific Grove, CA: Thomson
627 Learning.
628 Cassou, C., Terray, L., & Phillips, A. S. (2005). Tropical Atlantic Influence on European Heat Waves.
629 *Journal of Climate*, *18*(15), 2805–2811. https://doi.org/10.1175/JCLI3506.1
630 Chang, P., Yamagata, T., Schopf, P., Behera, S. K., Carton, J., Kessler, W. S., et al. (2006). Climate
631 Fluctuations of Tropical Coupled Systems—The Role of Ocean Dynamics. *Journal of Climate*,
632 *19*(20), 5122–5174. https://doi.org/10.1175/JCLI3903.1
633 Change, I. P. on C. (2012). *Managing the Risks of Extreme Events and Disasters to Advance Climate*
634 *Change Adaptation: Special Report of the Intergovernmental Panel on Climate Change*.
635 Cambridge University Press.
636 Ciais, P., Reichstein, M., Viovy, N., Granier, A., Ogée, J., Allard, V., et al. (2005). Europe-wide reduction in
637 primary productivity caused by the heat and drought in 2003. *Nature*, *437*(7058), 529–533.
638 https://doi.org/10.1038/nature03972
639 Dai, A., & Zhao, T. (2017). Uncertainties in historical changes and future projections of drought. Part I:
640 estimates of historical drought changes. *Climatic Change*, *144*(3), 519–533.
641 https://doi.org/10.1007/s10584-016-1705-2
642 Ding, S., Chen, W., Feng, J., & Graf, H.-F. (2017). Combined Impacts of PDO and Two Types of La Niña on
643 Climate Anomalies in Europe. *Journal of Climate*, *30*(9), 3253–3278.
644 https://doi.org/10.1175/JCLI-D-16-0376.1
645 Dittus, A. J., Karoly, D. J., Donat, M. G., Lewis, S. C., & Alexander, L. V. (2018). Understanding the role of
646 sea surface temperature-forcing for variability in global temperature and precipitation
647 extremes. *Weather and Climate Extremes*, *21*, 1–9. https://doi.org/10.1016/j.wace.2018.06.002

Dong, L., Mitra, C., Greer, S., Burt, E., Dong, L., Mitra, C., et al. (2018). The Dynamical Linkage of Atmospheric Blocking to Drought, Heatwave and Urban Heat Island in Southeastern US: A Multi-Scale Case Study. *Atmosphere*, *9*(1), 33. https://doi.org/10.3390/atmos9010033

Dulière, V., Zhang, Y., & Salathé, E. P. (2013). Changes in Twentieth-Century Extreme Temperature and Precipitation over the Western United States Based on Observations and Regional Climate Model Simulations. *Journal of Climate*, *26*(21), 8556–8575. https://doi.org/10.1175/JCLI-D-12-00818.1

Feng, S., Hao, Z., Zhang, X., & Hao, F. (2019). Probabilistic evaluation of the impact of compound dry-hot events on global maize yields. *Science of The Total Environment*, *689*, 1228–1234. https://doi.org/10.1016/j.scitotenv.2019.06.373

Filippi, L., Palazzi, E., von Hardenberg, J., & Provenzale, A. (2014). Multidecadal Variations in the Relationship between the NAO and Winter Precipitation in the Hindu Kush–Karakoram. *Journal of Climate*, *27*(20), 7890–7902. https://doi.org/10.1175/JCLI-D-14-00286.1

Guerreiro, S. B., Dawson, R. J., Kilsby, C., Lewis, E., & Ford, A. (2018). Future heat-waves, droughts and floods in 571 European cities. *Environmental Research Letters*, *13*(3), 034009. https://doi.org/10.1088/1748-9326/aaaad3

Hao, Z., AghaKouchak, A., & Phillips, T. J. (2013). Changes in concurrent monthly precipitation and temperature extremes. *Environmental Research Letters*, *8*(3), 034014. https://doi.org/10.1088/1748-9326/8/3/034014

Hao, Z., Hao, F., Singh, V. P., Xia, Y., Shi, C., & Zhang, X. (2018). A multivariate approach for statistical assessments of compound extremes. *Journal of Hydrology*, *565*, 87–94. https://doi.org/10.1016/j.jhydrol.2018.08.025

Hao, Z., Hao, F., Singh, V. P., & Zhang, X. (2018). Quantifying the relationship between compound dry and hot events and El Niño–southern Oscillation (ENSO) at the global scale. *Journal of Hydrology*, *567*, 332–338. https://doi.org/10.1016/j.jhydrol.2018.10.022

Hao, Z., Hao, F., Singh, V. P., & Zhang, X. (2019). Statistical prediction of the severity of compound dry-hot events based on El Niño-Southern Oscillation. *Journal of Hydrology*, *572*, 243–250. https://doi.org/10.1016/j.jhydrol.2019.03.001

Hirons, L., & Klingaman, N. (2015). *El Niño 2015/2016: impact analysis of past El Niños* (Report). Evidence on Demand. Retrieved from http://dx.doi.org/10.12774/eod_cr.august2015.hironsletal

Hurrell, J. W., Kushnir, Y., & Visbeck, M. (2001). The North Atlantic Oscillation. *Science*, *291*(5504), 603–605. https://doi.org/10.1126/science.1058761

Kamae, Y., Shiogama, H., Imada, Y., Mori, M., Arakawa, O., Mizuta, R., et al. (2017). Forced response and internal variability of summer climate over western North America. *Climate Dynamics*, *49*(1), 403–417. https://doi.org/10.1007/s00382-016-3350-x

Knippertz, P., Ulbrich, U., Marques, F., & Corte-Real, J. (2003). Decadal changes in the link between El Niño and springtime North Atlantic oscillation and European–North African rainfall. *International Journal of Climatology*, *23*(11), 1293–1311. https://doi.org/10.1002/joc.944

Lee, E., Bieda, R., Shanmugasundaram, J., & Richter, H. B. (2016). Land surface and atmospheric conditions associated with heat waves over the Chickasaw Nation in the South Central United States. *Journal of Geophysical Research: Atmospheres*, *121*(11), 6284–6298. https://doi.org/10.1002/2015JD024659

Leonard, M., Westra, S., Phatak, A., Lambert, M., Hurk, B. van den, McInnes, K., et al. (2014). A compound event framework for understanding extreme impacts. *Wiley Interdisciplinary Reviews: Climate Change*, *5*(1), 113–128. https://doi.org/10.1002/wcc.252

Lindsey, J. K. (2000). *Applying Generalized Linear Models*. Springer Science & Business Media.

694 Mahlstein, I., Martius, O., Chevalier, C., & Ginsbourger, D. (2012). Changes in the odds of extreme events
695 in the Atlantic basin depending on the position of the extratropical jet. *Geophysical Research*
696 *Letters*, *39*(22). https://doi.org/10.1029/2012GL053993
697 Mallakpour, I., & Villarini, G. (2016). Investigating the relationship between the frequency of flooding
698 over the central United States and large-scale climate. *Advances in Water Resources*, *92*, 159–
699 171. https://doi.org/10.1016/j.advwatres.2016.04.008
700 Martens, B., Waegeman, W., Dorigo, W. A., Verhoest, N. E. C., & Miralles, D. G. (2018). Terrestrial
701 evaporation response to modes of climate variability. *Npj Climate and Atmospheric Science*, *1*(1),
702 1–7. https://doi.org/10.1038/s41612-018-0053-5
703 Maurer, E. P., Wood, A. W., Adam, J. C., Lettenmaier, D. P., & Nijssen, B. (2002). A Long-Term
704 Hydrologically Based Dataset of Land Surface Fluxes and States for the Conterminous United
705 States. *Journal of Climate*, *15*(22), 3237–3251. https://doi.org/10.1175/1520-
706 0442(2002)015<3237:ALTHBD>2.0.CO;2
707 Mazdiyasni, O., & AghaKouchak, A. (2015). Substantial increase in concurrent droughts and heatwaves in
708 the United States. *Proceedings of the National Academy of Sciences*, *112*(37), 11484–11489.
709 https://doi.org/10.1073/pnas.1422945112
710 McCabe, G. J., Palecki, M. A., & Betancourt, J. L. (2004). Pacific and Atlantic Ocean influences on
711 multidecadal drought frequency in the United States. *Proceedings of the National Academy of*
712 *Sciences*, *101*(12), 4136–4141. https://doi.org/10.1073/pnas.0306738101
713 McCullagh, P., & Nelder, J. A. (1989). Generalized linear models., 2nd edn.(Chapman and Hall: London).
714 *Standard Book on Generalized Linear Models*.
715 McDonald, J. H. (2009). *Handbook of Biological Statistics*. Sparky House Publishing.
716 McKee, T. B., Doesken, N. J., & Kleist, J. (n.d.). THE RELATIONSHIP OF DROUGHT FREQUENCY AND
717 DURATION TO TIME SCALES, 6.

McPhaden, M. J., Zebiak, S. E., & Glantz, M. H. (2006). ENSO as an Integrating Concept in Earth Science. *Science*, *314*(5806), 1740–1745. https://doi.org/10.1126/science.1132588

Meyers, G., McIntosh, P., Pigot, L., & Pook, M. (2007). The Years of El Niño, La Niña, and Interactions with the Tropical Indian Ocean. *Journal of Climate*, *20*(13), 2872–2880. https://doi.org/10.1175/JCLI4152.1

Min, S.-K., Cai, W., & Whetton, P. (2013). Influence of climate variability on seasonal extremes over Australia. *Journal of Geophysical Research: Atmospheres*, *118*(2), 643–654. https://doi.org/10.1002/jgrd.50164

Miralles, D. G., Berg, M. J. van den, Gash, J. H., Parinussa, R. M., Jeu, R. A. M. de, Beck, H. E., et al. (2014). El Niño–La Niña cycle and recent trends in continental evaporation. *Nature Climate Change*, *4*(2), 122–126. https://doi.org/10.1038/nclimate2068

Miralles, D. G., Teuling, A. J., Heerwaarden, C. C. van, & Arellano, J. V.-G. de. (2014). Mega-heatwave temperatures due to combined soil desiccation and atmospheric heat accumulation. *Nature Geoscience*, *7*(5), 345–349. https://doi.org/10.1038/ngeo2141

Miralles, D. G., Gentine, P., Seneviratne, S. I., & Teuling, A. J. (2019). Land–atmospheric feedbacks during droughts and heatwaves: state of the science and current challenges. *Annals of the New York Academy of Sciences*, *1436*(1), 19–35. https://doi.org/10.1111/nyas.13912

Mishra, A. K., & Singh, V. P. (2010). A review of drought concepts. *Journal of Hydrology*, *391*(1), 202–216. https://doi.org/10.1016/j.jhydrol.2010.07.012

Mishra, A. K., & Singh, V. P. (2011). Drought modeling – A review. *Journal of Hydrology*, *403*(1), 157–175. https://doi.org/10.1016/j.jhydrol.2011.03.049

Mishra, V., Thirumalai, K., Singh, D., & Aadhar, S. (2020). Future exacerbation of hot and dry summer monsoon extremes in India. *Npj Climate and Atmospheric Science*, *3*(1), 1–9. https://doi.org/10.1038/s41612-020-0113-5

742 Mukherjee, S., Mishra, A., & Trenberth, K. E. (2018). Climate Change and Drought: a Perspective on
743 Drought Indices. *Current Climate Change Reports*, *4*(2), 145–163.
744 https://doi.org/10.1007/s40641-018-0098-x
745 Newman, M., Alexander, M. A., Ault, T. R., Cobb, K. M., Deser, C., Di Lorenzo, E., et al. (2016). The Pacific
746 Decadal Oscillation, Revisited. *Journal of Climate*, *29*(12), 4399–4427.
747 https://doi.org/10.1175/JCLI-D-15-0508.1
748 Park, T.-W., Deng, Y., & Cai, M. (2012). Feedback attribution of the El Niño–Southern Oscillation–related
749 atmospheric and surface temperature anomalies. *Journal of Geophysical Research:*
750 *Atmospheres*, *117*(D23). https://doi.org/10.1029/2012JD018468
751 Pepler, A., Dowdy, A., & Hope, P. (2018). A global climatology of surface anticyclones, their variability,
752 associated drivers and long-term trends. *Climate Dynamics*. https://doi.org/10.1007/s00382-
753 018-4451-5
754 Perkins, S. E., Alexander, L. V., & Nairn, J. R. (2012). Increasing frequency, intensity and duration of
755 observed global heatwaves and warm spells. *Geophysical Research Letters*, *39*(20).
756 https://doi.org/10.1029/2012GL053361
757 Perkins, Sarah E., Argüeso, D., & White, C. J. (2015). Relationships between climate variability, soil
758 moisture, and Australian heatwaves. *Journal of Geophysical Research: Atmospheres*, *120*(16),
759 8144–8164. https://doi.org/10.1002/2015JD023592
760 Peterson, T. C., Heim, R. R., Hirsch, R., Kaiser, D. P., Brooks, H., Diffenbaugh, N. S., et al. (2013).
761 Monitoring and Understanding Changes in Heat Waves, Cold Waves, Floods, and Droughts in the
762 United States: State of Knowledge. *Bulletin of the American Meteorological Society*, *94*(6), 821–
763 834. https://doi.org/10.1175/BAMS-D-12-00066.1

764 Poumadère, M., Mays, C., Le Mer, S., & Blong, R. (2005). The 2003 heat wave in France: dangerous
765 climate change here and now. *Risk Analysis: An Official Publication of the Society for Risk*
766 *Analysis*, *25*(6), 1483–1494. https://doi.org/10.1111/j.1539-6924.2005.00694.x
767 Rajagopalan, B., Cook, E., Lall, U., & Ray, B. K. (2000). Spatiotemporal Variability of ENSO and SST
768 Teleconnections to Summer Drought over the United States during the Twentieth Century.
769 *Journal of Climate*, *13*(24), 4244–4255. https://doi.org/10.1175/1520-
770 0442(2000)013<4244:SVOEAS>2.0.CO;2
771 Saji, N. H., & Yamagata, T. (2003). Possible impacts of Indian Ocean Dipole mode events on global
772 climate. *Climate Research*, *25*(2), 151–169. https://doi.org/10.3354/cr025151
773 Santanello, J. A., Dirmeyer, P. A., Ferguson, C. R., Findell, K. L., Tawfik, A. B., Berg, A., et al. (2017). Land–
774 Atmosphere Interactions: The LoCo Perspective. *Bulletin of the American Meteorological Society*,
775 *99*(6), 1253–1272. https://doi.org/10.1175/BAMS-D-17-0001.1
776 Schamm, K., Ziese, M., Raykova, K., Becker, A., Finger, P., Meyer-Christoffer, A., & Schneider, U. (2015).
777 *GPCC full data daily version 1.0 at 1.0: Daily land-surface precipitation from rain-gauges built on*
778 *GTS-based and historic data*. DOI.
779 Seager, R., Naik, N., & Vecchi, G. A. (2010). Thermodynamic and Dynamic Mechanisms for Large-Scale
780 Changes in the Hydrological Cycle in Response to Global Warming. *Journal of Climate*, *23*(17),
781 4651–4668. https://doi.org/10.1175/2010JCLI3655.1
782 Seneviratne, S. I., Corti, T., Davin, E. L., Hirschi, M., Jaeger, E. B., Lehner, I., et al. (2010). Investigating soil
783 moisture–climate interactions in a changing climate: A review. *Earth-Science Reviews*, *99*(3),
784 125–161. https://doi.org/10.1016/j.earscirev.2010.02.004
785 Seneviratne, S. I., Nicholls, N., Easterling, D., Goodess, C. M., Kanae, S., Kossin, J., et al. (2012). Changes
786 in climate extremes and their impacts on the natural physical environment. *Managing the Risks*
787 *of Extreme Events and Disasters to Advance Climate Change Adaptation: Special Report of the*

Intergovernmental Panel on Climate Change, 109–230. https://doi.org/10.1017/CBO9781139177245.006

Stéfanon, M., Drobinski, P., D'Andrea, F., Lebeaupin-Brossier, C., & Bastin, S. (2014). Soil moisture-temperature feedbacks at meso-scale during summer heat waves over Western Europe. *Climate Dynamics*, *42*(5), 1309–1324. https://doi.org/10.1007/s00382-013-1794-9

Sun, Q., Miao, C., AghaKouchak, A., & Duan, Q. (2016). Century-scale causal relationships between global dry/wet conditions and the state of the Pacific and Atlantic Oceans. *Geophysical Research Letters*, *43*(12), 6528–6537. https://doi.org/10.1002/2016GL069628

Sun, Q., Miao, C., Duan, Q., Ashouri, H., Sorooshian, S., & Hsu, K.-L. (2018). A Review of Global Precipitation Data Sets: Data Sources, Estimation, and Intercomparisons. *Reviews of Geophysics*, *56*(1), 79–107. https://doi.org/10.1002/2017RG000574

Trenberth, K. E., Stepaniak, D. P., & Caron, J. M. (2000). The Global Monsoon as Seen through the Divergent Atmospheric Circulation. *Journal of Climate*, *13*(22), 3969–3993. https://doi.org/10.1175/1520-0442(2000)013<3969:TGMAST>2.0.CO;2

Trenberth, K. E., Caron, J. M., Stepaniak, D. P., & Worley, S. (2002). Evolution of El Niño–Southern Oscillation and global atmospheric surface temperatures. *Journal of Geophysical Research: Atmospheres*, *107*(D8), AAC 5-1. https://doi.org/10.1029/2000JD000298

Trouet, V., Babst, F., & Meko, M. (2018). Recent enhanced high-summer North Atlantic Jet variability emerges from three-century context. *Nature Communications*, *9*(1), 180. https://doi.org/10.1038/s41467-017-02699-3

Villarini, G., Vecchi, G. A., & Smith, J. A. (2010). Modeling the Dependence of Tropical Storm Counts in the North Atlantic Basin on Climate Indices. *Monthly Weather Review*, *138*(7), 2681–2705. https://doi.org/10.1175/2010MWR3315.1

Walz, M. A., Befort, D. J., Kirchner-Bossi, N. O., Ulbrich, U., & Leckebusch, G. C. (2018). Modelling serial clustering and inter-annual variability of European winter windstorms based on large-scale drivers. *International Journal of Climatology*, *38*(7), 3044–3057. https://doi.org/10.1002/joc.5481

Wang, C., Deser, C., Yu, J.-Y., DiNezio, P., & Clement, A. (2017). El Niño and Southern Oscillation (ENSO): A Review. In P. W. Glynn, D. P. Manzello, & I. C. Enochs (Eds.), *Coral Reefs of the Eastern Tropical Pacific: Persistence and Loss in a Dynamic Environment* (pp. 85–106). Dordrecht: Springer Netherlands. https://doi.org/10.1007/978-94-017-7499-4_4

Webb, R., Rosenzweig, C. E., & Levine, E. R. (2000). Global Soil Texture and Derived Water-Holding Capacities (Webb et al.). *ORNL DAAC*. https://doi.org/10.3334/ORNLDAAC/548

Wegren, S. K. (2011). Food Security and Russia's 2010 Drought. *Eurasian Geography and Economics*, *52*(1), 140–156. https://doi.org/10.2747/1539-7216.52.1.140

Wells, N., Goddard, S., & Hayes, M. J. (2004). A Self-Calibrating Palmer Drought Severity Index. *Journal of Climate*, *17*(12), 2335–2351. https://doi.org/10.1175/1520-0442(2004)017<2335:ASPDSI>2.0.CO;2

Whan, K., Zscheischler, J., Orth, R., Shongwe, M., Rahimi, M., Asare, E. O., & Seneviratne, S. I. (2015). Impact of soil moisture on extreme maximum temperatures in Europe. *Weather and Climate Extremes*, *9*, 57–67. https://doi.org/10.1016/j.wace.2015.05.001

Wu, X., Hao, Z., Hao, F., & Zhang, X. (2019). Variations of compound precipitation and temperature extremes in China during 1961–2014. *Science of The Total Environment*, *663*, 731–737. https://doi.org/10.1016/j.scitotenv.2019.01.366

Xiao, M., Zhang, Q., & Singh, V. P. (2015). Influences of ENSO, NAO, IOD and PDO on seasonal precipitation regimes in the Yangtze River basin, China. *International Journal of Climatology*, *35*(12), 3556–3567. https://doi.org/10.1002/joc.4228

Yoon, J.-H., Kravitz, B., Rasch, P. J., Simon Wang, S.-Y., Gillies, R. R., & Hipps, L. (2015). Extreme Fire Season in California: A Glimpse Into the Future? *Bulletin of the American Meteorological Society*, *96*(12), S5–S9. https://doi.org/10.1175/BAMS-D-15-00114.1

Yu, E., King, M. P., Sobolowski, S., Otterå, O. H., & Gao, Y. (2018). Asian droughts in the last millennium: a search for robust impacts of Pacific Ocean surface temperature variabilities. *Climate Dynamics*, *50*(11), 4671–4689. https://doi.org/10.1007/s00382-017-3897-1

Zampieri, M., Ceglar, A., Dentener, F., & Toreti, A. (2017). Wheat yield loss attributable to heat waves, drought and water excess at the global, national and subnational scales. *Environmental Research Letters*, *12*(6), 064008. https://doi.org/10.1088/1748-9326/aa723b

Zhou, S., Williams, A. P., Berg, A. M., Cook, B. I., Zhang, Y., Hagemann, S., et al. (2019). Land–atmosphere feedbacks exacerbate concurrent soil drought and atmospheric aridity. *Proceedings of the National Academy of Sciences*, *116*(38), 18848–18853. https://doi.org/10.1073/pnas.1904955116

Ziese, M., Rauthe-Schöch, A., Becker, A., Finger, P., Meyer-Christoffer, A., & Schneider, U. (2018). *GPCC full data daily version. 2018 at 1.0◦: Daily land-surface precipitation from rain-gauges built on GTS-based and historic data*. DOI.

ZOBLER, L. (1986). A world soil file grobal climate modeling. *NASA Tech. Memo*, *32*. Retrieved from https://ci.nii.ac.jp/naid/10004560598/

Zscheischler, J., Westra, S., Hurk, B. J. J. M. van den, Seneviratne, S. I., Ward, P. J., Pitman, A., et al. (2018). Future climate risk from compound events. *Nature Climate Change*, *8*(6), 469. https://doi.org/10.1038/s41558-018-0156-3

Figure 1.

(a)

Temperature
Heatwave threshold
scPDSI
Extreme drought threshold

Temperature (°C)

scPDSI

(b)

Compound Drought and Heat wave (CDHW) event

Heatwave threshold

Extreme drought threshold

Temperature (°C)

scPDSI

Day of Year

Figure 2.

Preliminary Model Selection

Gridded Seasonal Precipitation

Gridded Seasonal Temperature

Potential Drivers

Seasonal mean of Nino3.4 (ENSO), PDO, and NAO

Percentage of grid-cells showing statistically significant (at 95 % confidence level) correlation with either precipitation or temperature or both

< 10%

NA

≥ 10%

Based on non-parametric spearman's rank correlation applied at each grid cell separately.

Selected Regional Drivers (RD)

RD-1	RD-2	RD-3	RD-4	RD-5	RD-6	RD-7
ENSO	PDO	NAO	ENSO+PDO	ENSO+NAO	PDO+NAO	ENSO+PDO +NAO

Seasonal CDHW Frequency

Poisson GLM Fitting

Stepwise AIC

Wald Test (at 95% confidence level)

Based on Poisson GLM applied at each grid cell separately.

Final Model Selection

Possible Combinations of Drivers or Models selected for each grid location within the region

RD-1	RD-2	RD-3	RD-4	RD-5	RD-6	RD-7
M1: ENSO	M2: PDO	M3: NAO	M1: ENSO, or M2: PDO, or M4: ENSO+PDO	M1: ENSO, or M3: NAO, or M5: ENSO+NAO	M2: PDO, or M3: NAO, or M6: PDO+NAO	M1 to M6, or M7: ENSO+PDO+NAO
or NA	or NA	or NA	or NA	or NA	or NA	or NA

Figure 3.

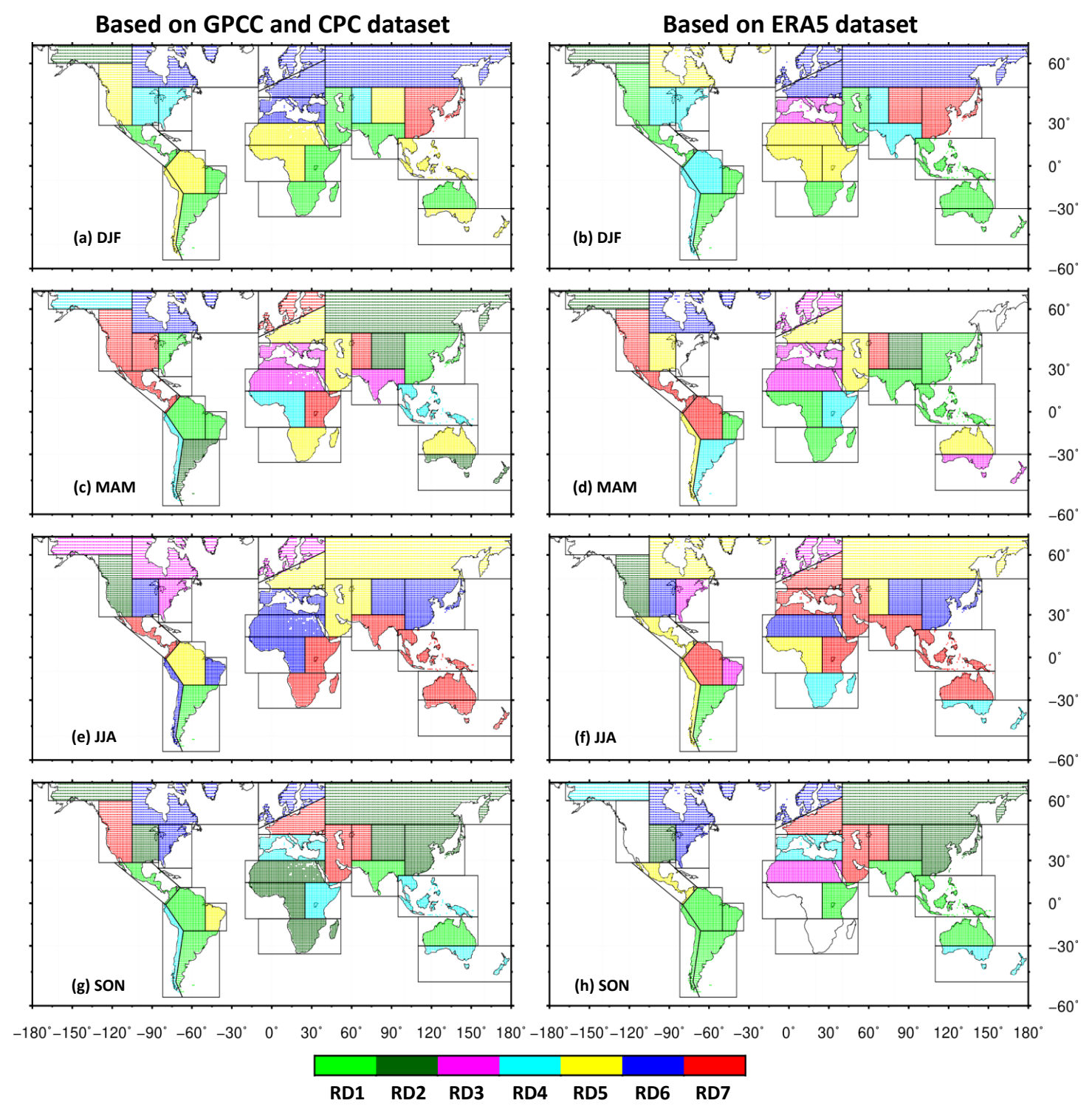
Based on GPCC and CPC dataset
Based on ERA5 dataset
(a) DJF
(b) DJF
(c) MAM
(d) MAM
(e) JJA
(f) JJA
(g) SON
(h) SON
60°
30°
0°
−30°
−60°
−180° −150° −120° −90° −60° −30° 0° 30° 60° 90° 120° 150° 180°
RD1 RD2 RD3 RD4 RD5 RD6 RD7

Figure 4.

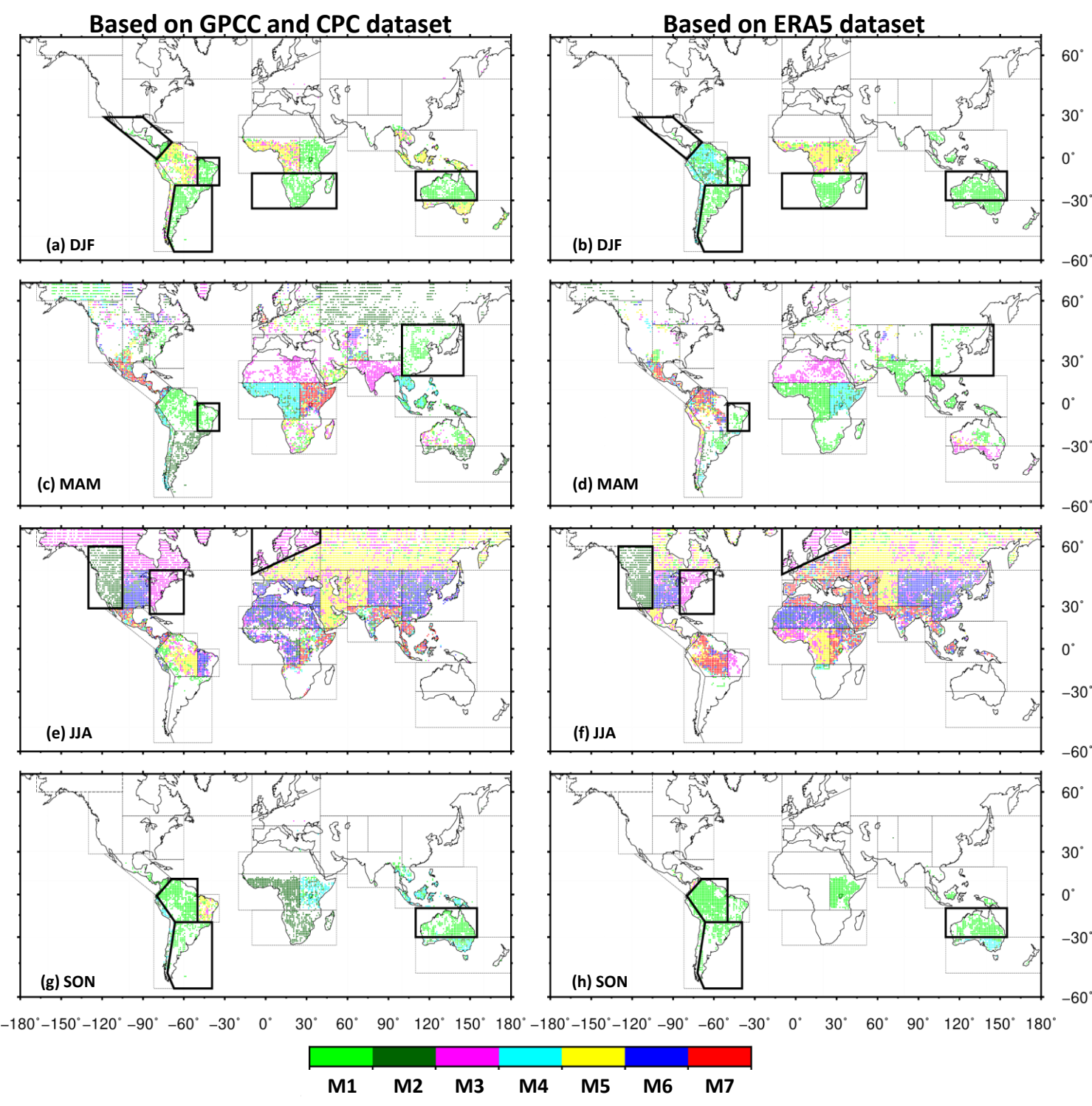
Based on GPCC and CPC dataset
Based on ERA5 dataset
(a) DJF
(b) DJF
(c) MAM
(d) MAM
(e) JJA
(f) JJA
(g) SON
(h) SON
60˚
30˚
0˚
–30˚
–60˚
–180˚ –150˚ –120˚ –90˚ –60˚ –30˚ 0˚ 30˚ 60˚ 90˚ 120˚ 150˚ 180˚
M1 M2 M3 M4 M5 M6 M7

Figure 5.

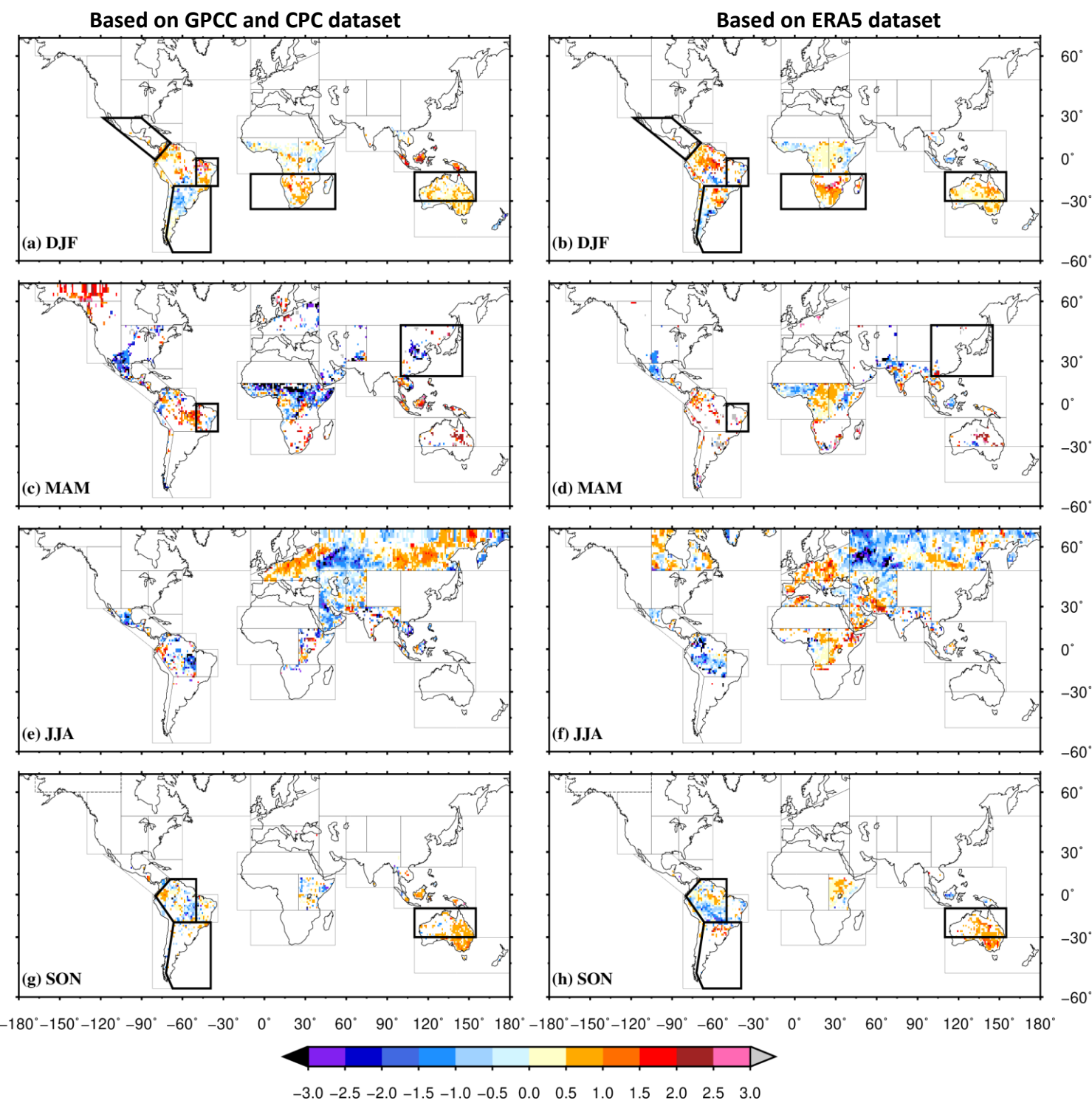
Based on GPCC and CPC dataset
Based on ERA5 dataset
(a) DJF
(b) DJF
(c) MAM
(d) MAM
(e) JJA
(f) JJA
(g) SON
(h) SON
60°
30°
0°
−30°
−60°
−180° −150° −120° −90° −60° −30° 0° 30° 60° 90° 120° 150° 180°
−3.0 −2.5 −2.0 −1.5 −1.0 −0.5 0.0 0.5 1.0 1.5 2.0 2.5 3.0

Figure 6.

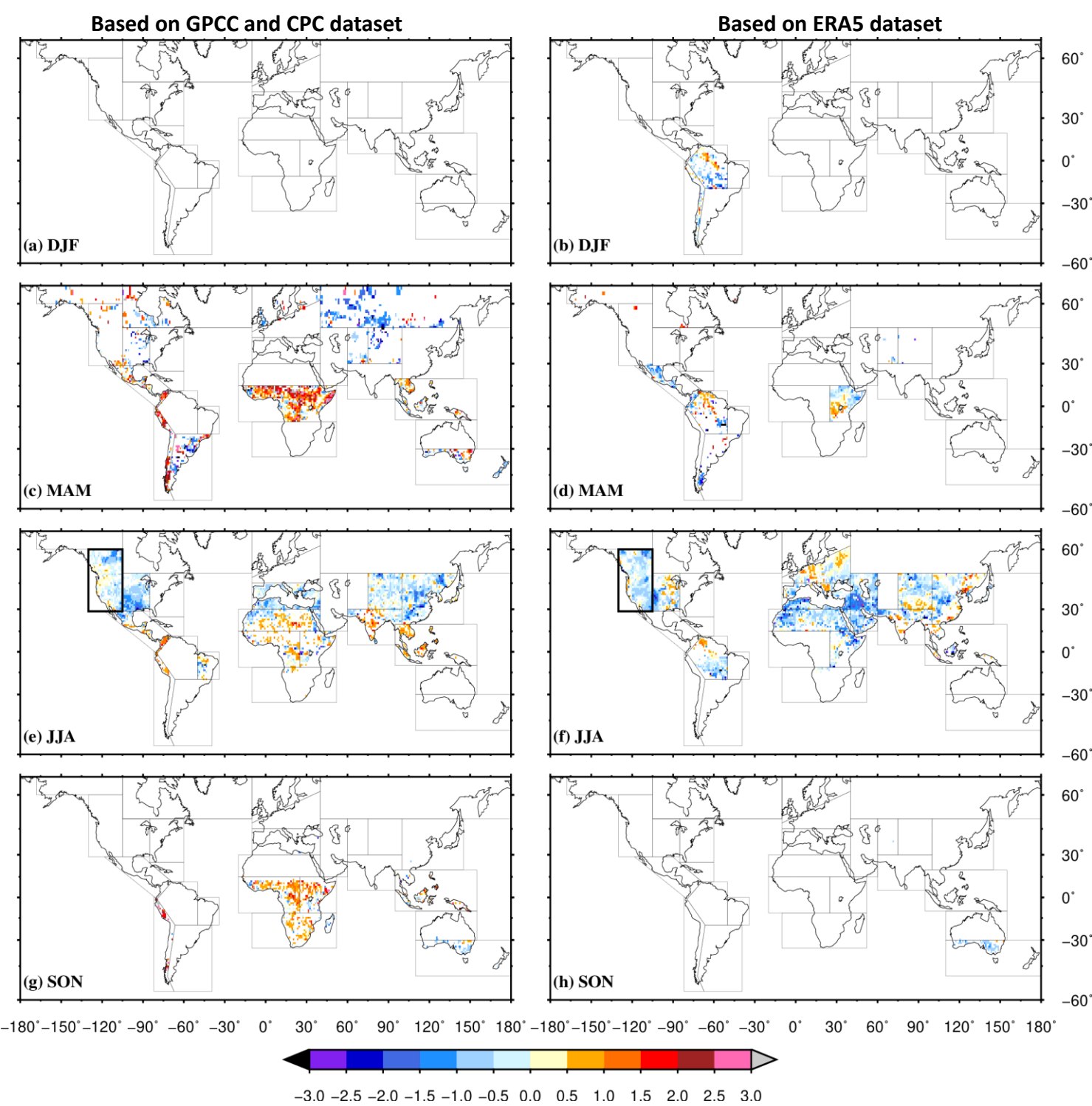
Based on GPCC and CPC dataset
Based on ERA5 dataset
(a) DJF
(b) DJF
(c) MAM
(d) MAM
(e) JJA
(f) JJA
(g) SON
(h) SON
60˚
30˚
0˚
−30˚
−60˚
−180˚ −150˚ −120˚ −90˚ −60˚ −30˚ 0˚ 30˚ 60˚ 90˚ 120˚ 150˚ 180˚
−3.0 −2.5 −2.0 −1.5 −1.0 −0.5 0.0 0.5 1.0 1.5 2.0 2.5 3.0

Figure 7.

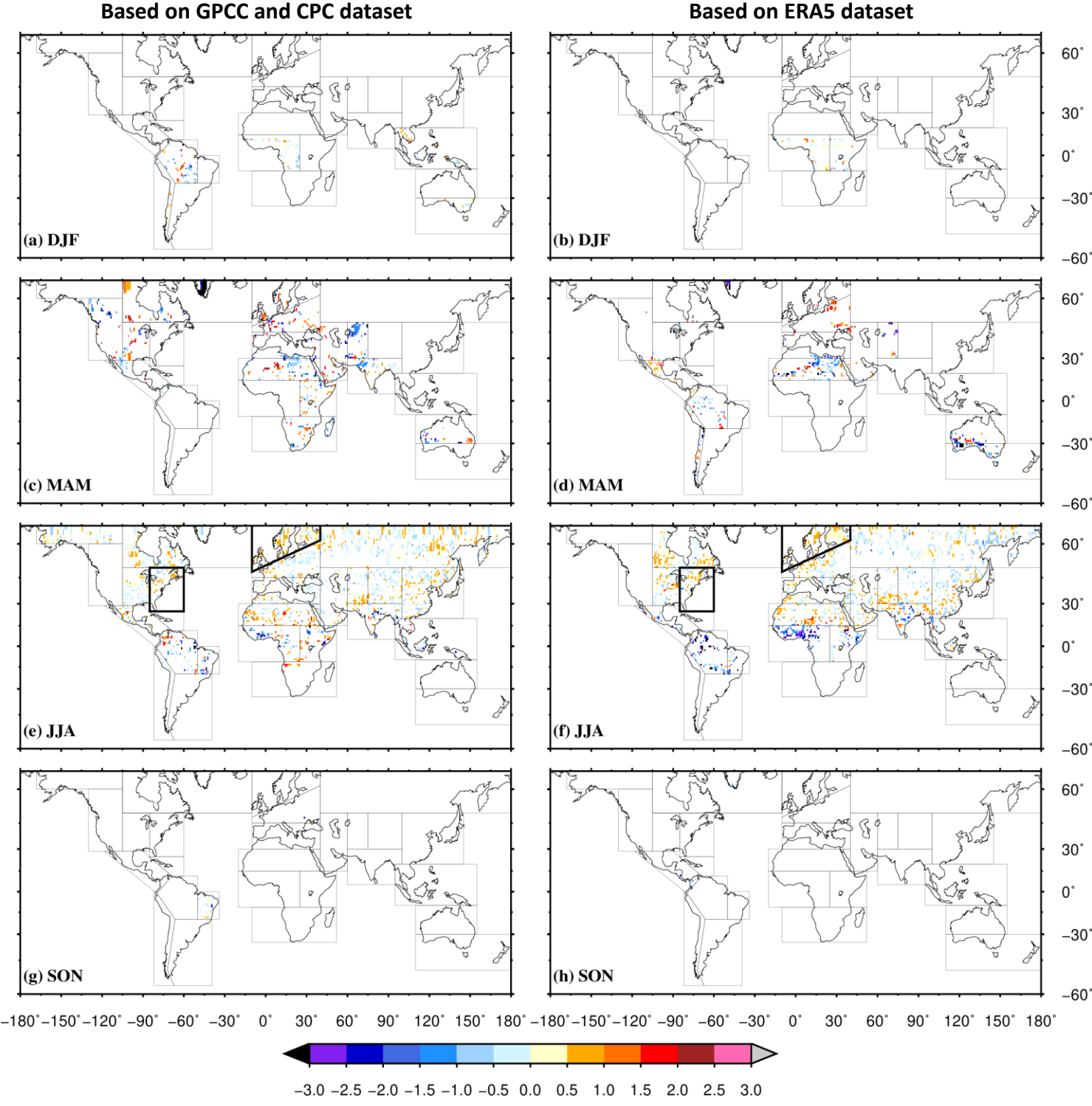
Based on GPCC and CPC dataset
Based on ERA5 dataset
(a) DJF
(b) DJF
(c) MAM
(d) MAM
(e) JJA
(f) JJA
(g) SON
(h) SON
60˚
30˚
0˚
−30˚
−60˚
−180˚ −150˚ −120˚ −90˚ −60˚ −30˚ 0˚ 30˚ 60˚ 90˚ 120˚ 150˚ 180˚
−3.0 −2.5 −2.0 −1.5 −1.0 −0.5 0.0 0.5 1.0 1.5 2.0 2.5 3.0

Figure 8.

El Niño

La Niña

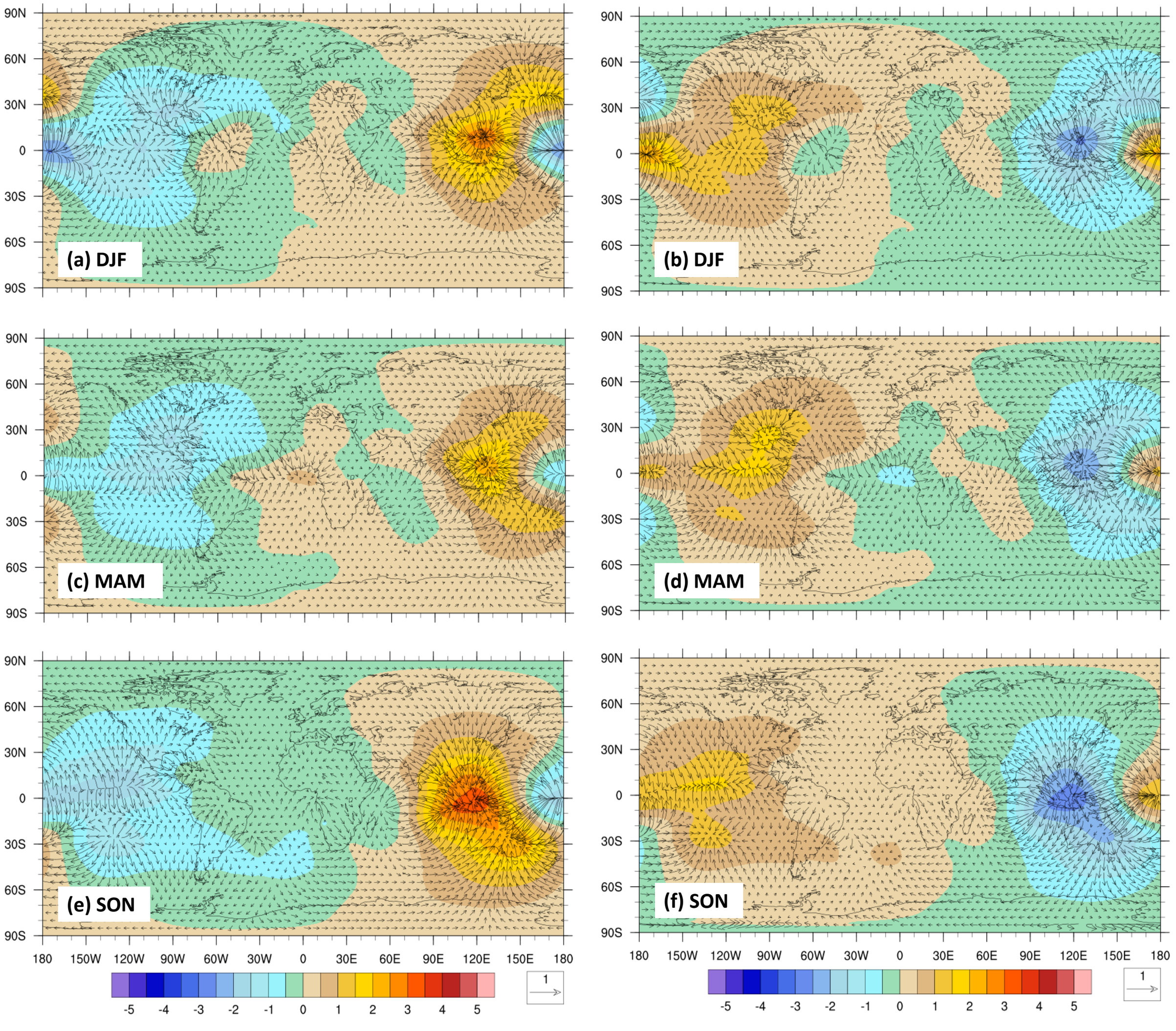

Figure 9.

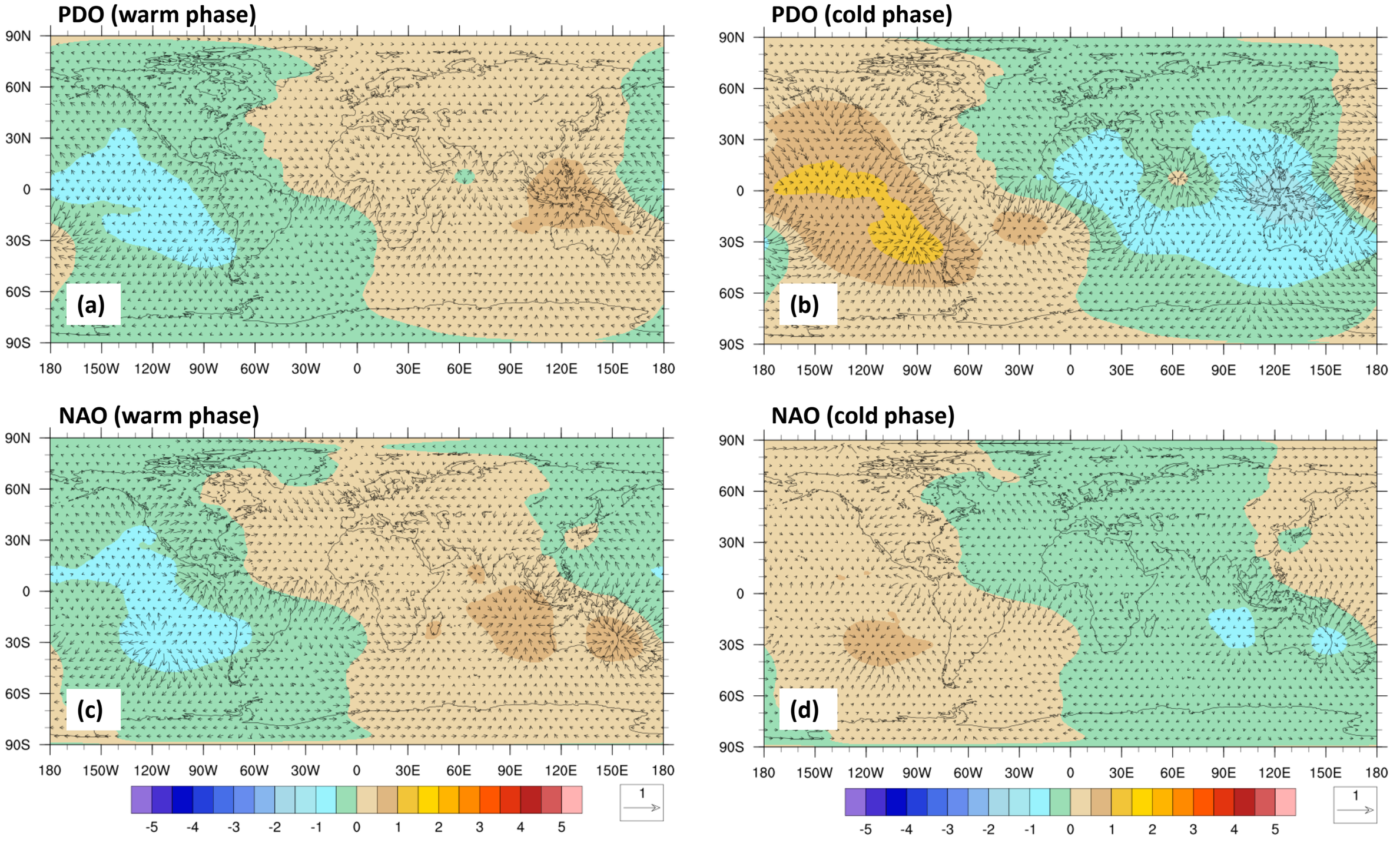
PDO (warm phase)
PDO (cold phase)
NAO (warm phase)
NAO (cold phase)
(a)
(b)
(c)
(d)
90N
60N
30N
0
30S
60S
90S
180 150W 120W 90W 60W 30W 0 30E 60E 90E 120E 150E 180
-5 -4 -3 -2 -1 0 1 2 3 4 5
1

Figure 10.

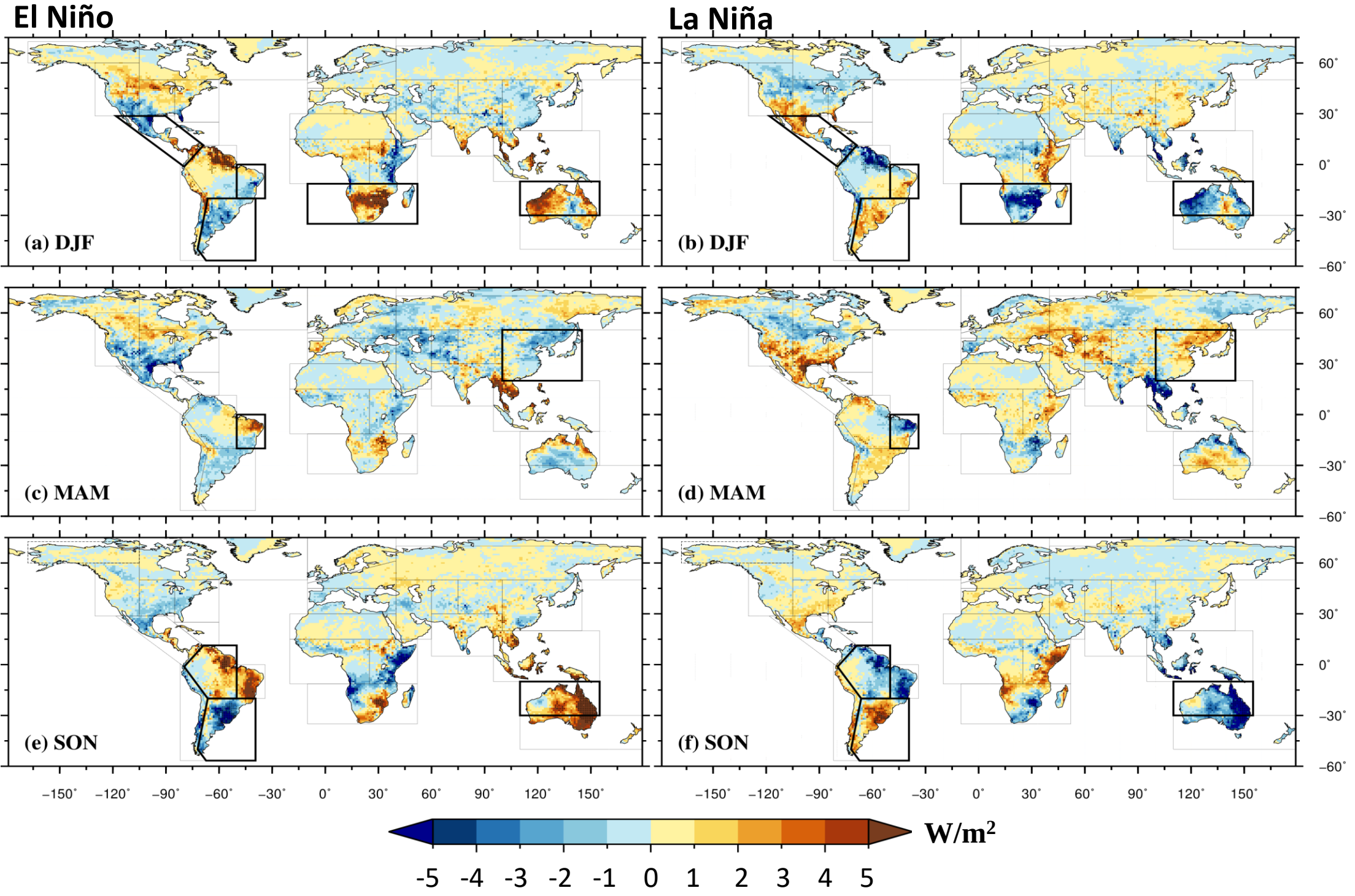
El Niño
La Niña
(a) DJF
(b) DJF
(c) MAM
(d) MAM
(e) SON
(f) SON
60°
30°
0°
-30°
-60°
-150° -120° -90° -60° -30° 0° 30° 60° 90° 120° 150°
W/m²
-5 -4 -3 -2 -1 0 1 2 3 4 5

Figure 11.

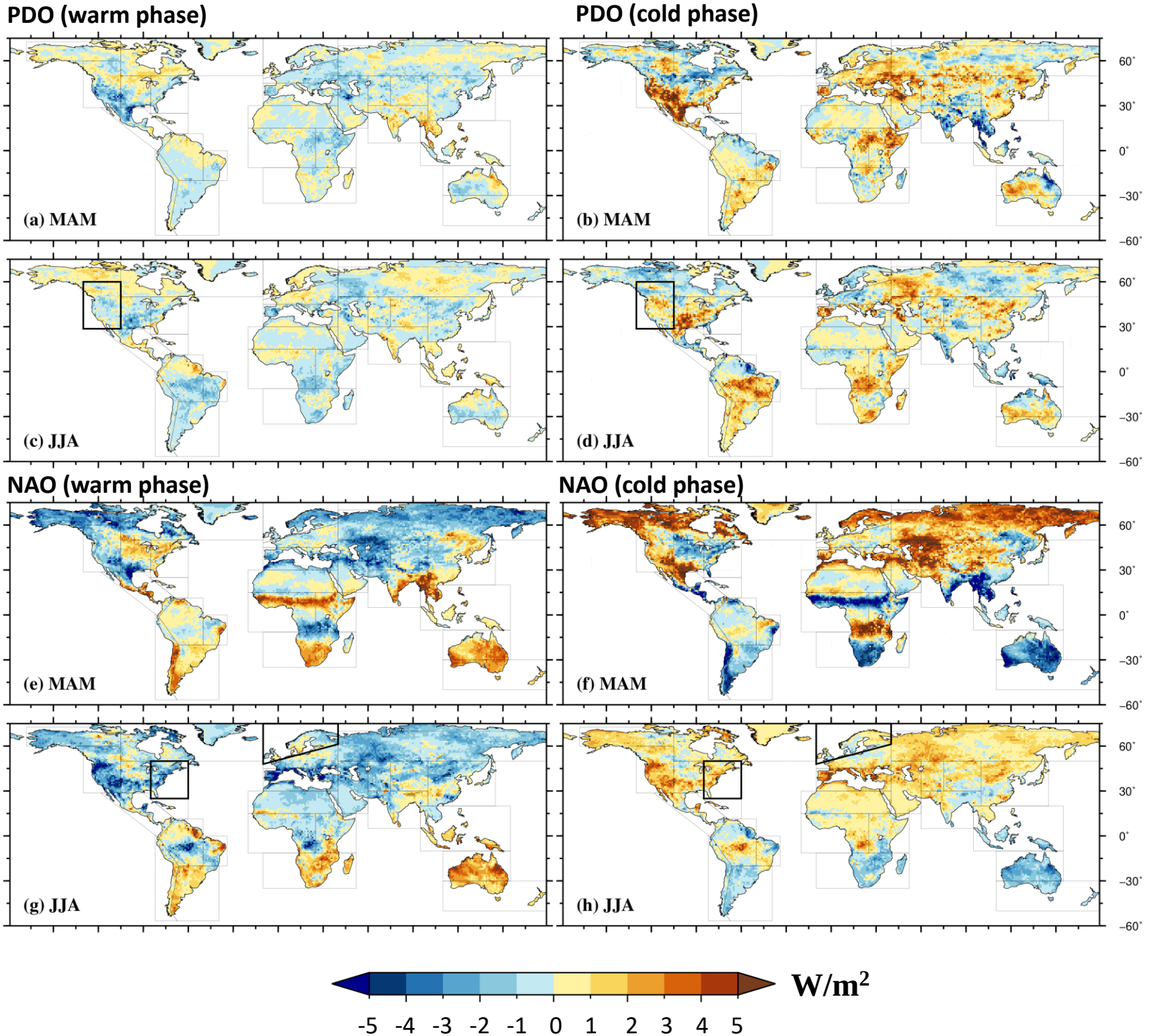
PDO (warm phase)
PDO (cold phase)
(a) MAM
(b) MAM
(c) JJA
(d) JJA
NAO (warm phase)
NAO (cold phase)
(e) MAM
(f) MAM
(g) JJA
(h) JJA
60°
30°
0°
-30°
-60°
W/m²
-5 -4 -3 -2 -1 0 1 2 3 4 5